



# Cluster Difference Imaging Photometric Survey. II. TOI 837: A Young Validated Planet in IC 2602

L. G. Bouma<sup>1</sup> , J. D. Hartman<sup>1</sup> , R. Brahm<sup>2,3</sup> , P. Evans<sup>4</sup> , K. A. Collins<sup>5</sup> , G. Zhou<sup>5</sup> , P. Sarkis<sup>6</sup> , S. N. Quinn<sup>5</sup> , J. de Leon<sup>7</sup> , J. Livingston<sup>7</sup> , C. Bergmann<sup>8,9</sup> , K. G. Stassun<sup>10,11</sup> , W. Bhatti<sup>1</sup> , J. N. Winn<sup>1</sup> , G. Á. Bakos<sup>1</sup> , L. Abe<sup>12</sup> , N. Crouzet<sup>13</sup> , G. Dransfield<sup>14</sup> , T. Guillot<sup>12</sup> , W. Marie-Sainte<sup>15</sup> , D. Mékarnia<sup>12</sup> , A. H. M. J. Triaud<sup>14</sup> , C. G. Tinney<sup>8</sup> , T. Henning<sup>6</sup> , N. Espinoza<sup>16</sup> , A. Jordán<sup>2,3</sup> , M. Barbieri<sup>17</sup> , S. Nandakumar<sup>17</sup> , T. Trifonov<sup>6</sup> , J. I. Vines<sup>18</sup> , M. Vuckovic<sup>19</sup> , C. Ziegler<sup>20</sup> , N. Law<sup>21</sup> , A. W. Mann<sup>21</sup> , G. R. Ricker<sup>22</sup> , R. Vanderspek<sup>22</sup> , S. Seager<sup>23</sup> , J. M. Jenkins<sup>24</sup> , C. J. Burke<sup>22</sup> , D. Dragomir<sup>25</sup> , A. M. Levine<sup>22</sup> , E. V. Quintana<sup>26</sup> , J. E. Rodriguez<sup>5</sup> , J. C. Smith<sup>24,27</sup> , and B. Wohler<sup>24,27</sup>

<sup>1</sup> Department of Astrophysical Sciences, Princeton University, 4 Ivy Lane, Princeton, NJ 08540, USA; [luke@astro.princeton.edu](mailto:luke@astro.princeton.edu)

<sup>2</sup> Facultad de Ingeniería y Ciencias, Universidad Adolfo Ibáñez, Av. Diagonal las Torres 2640, Peñalolén, Santiago, Chile

<sup>3</sup> Millennium Institute for Astrophysics, Chile

<sup>4</sup> El Sauce Observatory, Coquimbo Province, Chile

<sup>5</sup> Center for Astrophysics|Harvard & Smithsonian, 60 Garden Street, Cambridge, MA 02138, USA

<sup>6</sup> Max-Planck-Institut für Astronomie, Königstuhl 17, Heidelberg D-69117, Germany

<sup>7</sup> Department of Astronomy, University of Tokyo, 7-3-1 Hongo, Bunkyo-ku, Tokyo 113-0033, Japan

<sup>8</sup> Exoplanetary Science at UNSW, School of Physics, UNSW Sydney, NSW 2052, Australia

<sup>9</sup> Deutsches Zentrum für Luft- und Raumfahrt, Münchener Str. 20, D-82234 Wessling, Germany

<sup>10</sup> Vanderbilt University, Department of Physics & Astronomy, 6301 Stevenson Center Lane, Nashville, TN 37235, USA

<sup>11</sup> Fisk University, Department of Physics, 1000 17th Avenue North, Nashville, TN 37208, USA

<sup>12</sup> Université Côte d'Azur, Observatoire de la Côte d'Azur, CNRS, Laboratoire Lagrange, Bd de l'Observatoire, CS 34229, F-06304 Nice cedex 4, France

<sup>13</sup> European Space Agency, European Space Research and Technology Centre (ESA/ESTEC), Keplerlaan 1, 2201 AZ Noordwijk, The Netherlands

<sup>14</sup> School of Physics & Astronomy, University of Birmingham, Edgbaston, Birmingham B15 2TT, UK

<sup>15</sup> Institut Paul Émile Victor, Concordia Station, Antarctica

<sup>16</sup> Space Telescope Science Institute, 3700 San Martin Drive, Baltimore, MD 21218, USA

<sup>17</sup> INCT, Universidad de Atacama, Calle Copayapu 485, Copiapó, Atacama, Chile

<sup>18</sup> Departamento de Astronomía, Universidad de Chile, Camino El Observatorio 1515, Las Condes, Santiago, Chile

<sup>19</sup> Instituto de Física y Astronomía, Universidad de Valparaíso, Casilla 5030, Valparaíso, Chile

<sup>20</sup> Dunlap Institute for Astronomy and Astrophysics, University of Toronto, 50 St. George Street, Toronto, Ontario M5S 3H4, Canada

<sup>21</sup> Department of Physics and Astronomy, The University of North Carolina at Chapel Hill, Chapel Hill, NC 27599-3255, USA

<sup>22</sup> Department of Physics and Kavli Institute for Astrophysics and Space Research, Massachusetts Institute of Technology, Cambridge, MA 02139, USA

<sup>23</sup> Department of Earth, Atmospheric, and Planetary Sciences, Massachusetts Institute of Technology, Cambridge, MA 02139, USA

<sup>24</sup> NASA Ames Research Center, Moffett Field, CA 94035, USA

<sup>25</sup> Department of Physics and Astronomy, University of New Mexico, Albuquerque, NM, USA

<sup>26</sup> NASA Goddard Space Flight Center, 8800 Greenbelt Road, Greenbelt, MD 20771, USA

<sup>27</sup> SETI Institute, Mountain View, CA 94043, USA

Received 2020 August 6; revised 2020 September 6; accepted 2020 September 16; published 2020 November 3

## Abstract

We report the discovery of TOI 837b and its validation as a transiting planet. We characterize the system using data from the NASA Transiting Exoplanet Survey Satellite mission, the ESA Gaia mission, ground-based photometry from El Sauce and ASTEP400, and spectroscopy from CHIRON, FEROS, and Veloce. We find that TOI 837 is a  $T = 9.9$  mag G0/F9 dwarf in the southern open cluster IC 2602. The star and planet are therefore  $35^{+11}_{-5}$  million years old. Combining the transit photometry with a prior on the stellar parameters derived from the cluster color–magnitude diagram, we find that the planet has an orbital period of 8.3 days and is slightly smaller than Jupiter ( $R_p = 0.77^{+0.09}_{-0.07} R_{\text{Jup}}$ ). From radial velocity monitoring, we limit  $M_p \sin i$  to less than  $1.20 M_{\text{Jup}}$  ( $3\sigma$ ). The transits either graze or nearly graze the stellar limb. Grazing transits are a cause for concern, as they are often indicative of astrophysical false-positive scenarios. Our follow-up data show that such scenarios are unlikely. Our combined multicolor photometry, high-resolution imaging, and radial velocities rule out hierarchical eclipsing binary scenarios. Background eclipsing binary scenarios, though limited by speckle imaging, remain a 0.2% possibility. TOI 837b is therefore a validated adolescent exoplanet. The planetary nature of the system can be confirmed or refuted through observations of the stellar obliquity and the planetary mass. Such observations may also improve our understanding of how the physical and orbital properties of exoplanets change in time.

*Unified Astronomy Thesaurus concepts:* [Exoplanets \(498\)](#); [Transits \(1711\)](#); [Exoplanet evolution \(491\)](#); [Stellar ages \(1581\)](#); [Young star clusters \(1833\)](#)

*Supporting material:* machine-readable table

## 1. Introduction

Over the first 100 million years of their lives, exoplanet systems are expected to undergo major physical and dynamical changes. For a typical Sun-like star, the protoplanetary disk disperses within roughly 1–10 million years (Mamajek 2009;

Dullemond & Monnier 2010; Fedele et al. 2010; Williams & Cieza 2011). Gas giants presumably finish accreting before the end of disk dispersal (Pollack et al. 1996). While rocky planets may form within only a few million years (Dauphas & Pourmand 2011), they can also undergo significant growth over

the next 10–100 million years through giant impacts (e.g., Kleine et al. 2009; König et al. 2011; Morbidelli et al. 2012; Raymond et al. 2014). The Moon, for instance, may have formed from debris ejected during a collision between the proto-Earth and a planetesimal during Earth’s first 100 million years (Cameron & Ward 1976; Canup & Asphaug 2001; Touboul et al. 2007).

A number of other processes are expected to shape young exoplanets. After accreting, planets with gaseous envelopes are thought to cool and contract, and their atmospheres are expected to undergo a mix of photoevaporation and core-powered mass loss (e.g., Fortney et al. 2007; Owen & Wu 2013; Fulton et al. 2017; Gupta & Schlichting 2019, 2020). Predicted timescales for photoevaporation and core-powered mass loss range from 10 million years to over 1 Gyr for typical transiting sub-Neptunes (Ginzburg et al. 2016; Owen & Wu 2017; King & Wheatley 2020). The relative importance of each process is set by the planetary surface gravity and the radiation environment. Both processes can be directly observed in favorable cases using the metastable 1083 nm He line (Mansfield et al. 2018; Oklopčić & Hirata 2018; Spake et al. 2018).

Beyond physical changes, dynamical changes are expected in the semimajor axes, eccentricities, and stellar obliquities of young planets. When the gas disk is present, the planetary semimajor axis is thought to change in step with the viscous evolution of the disk (Lin et al. 1996). High-eccentricity migration processes including planet–planet scattering, secular chaos, and Kozai–Lidov oscillations can also occur (e.g., Fabrycky & Tremaine 2007; Chatterjee et al. 2008; Lithwick & Wu 2014). The circularization timescale is thought to be such that for any giant planets that do migrate early, their orbits should circularize within 100 million years (Zahn 1977; Bonomo et al. 2017).

Finding and understanding systems undergoing these evolutionary changes is a major goal in contemporary exoplanet research. To identify stars younger than 1 Gyr, for example, a number of direct and indirect methods are available (Soderblom 2010). The traditional approach is to isochronally age-date coeval groups of stars, hereafter referred to as “clusters” (e.g., Lada & Lada 2003; Zuckerman & Song 2004; Krumholz et al. 2019). Young field stars can also be identified isochronally, provided that they are sufficiently massive (Berger et al. 2020). Other age indicators include stellar rotation periods, the abundance of photospheric lithium, and chromospheric diagnostics such as calcium emission and broadband UV emission. Studies by, for instance, Sanchis-Ojeda et al. (2013) and David et al. (2018) have combined these methods to age-date individual field stars hosting transiting planets. Many of these latter methods were summarized by Mamajek & Hillenbrand (2008) and have since been calibrated by, e.g., Irwin & Bouvier (2009), Barnes et al. (2015), Meibom et al. (2015), Angus et al. (2015), and Curtis et al. (2019b) for stellar rotation, Žerjal et al. (2017) for chromospheric activity, and Berger et al. (2018) and Žerjal et al. (2019) for lithium abundance.

To date, a few dozen planets in clusters have been detected, and fewer still have been closely characterized. Despite the challenges of starspot-induced radial velocity (RV) variations, RV surveys found early success in the Hyades, NGC 2423, Praesepe, and M67 (Lovis & Mayor 2007; Sato et al. 2007; Quinn et al. 2012; Malavolta et al. 2016; Brucalassi et al. 2017).

RV surveys of highly active pre-main-sequence (PMS) stars in Taurus also led to the youngest hot Jupiters yet reported orbiting V830 Tau, TAP 26, and CI Tau (Donati et al. 2016; Johns-Krull et al. 2016; Yu et al. 2017; Biddle et al. 2018; Flagg et al. 2019). The planetary nature of at least two of these signals has been debated (Damasso et al. 2020; Donati et al. 2020).

The transit method was comparatively slow in catching up. Early deep transit searches of open clusters by many groups did not yield definitive planet detections (Mochejska et al. 2005, 2006; Burke et al. 2006; Aigrain et al. 2007; Irwin et al. 2007; Miller et al. 2008; Pepper et al. 2008; Hartman et al. 2009). These searches were typically sensitive to planets larger than Jupiter, on  $\lesssim 3$  day orbital periods. Hot-Jupiter occurrence rate limits were derived at the  $\lesssim 5\%$  level (e.g., Burke et al. 2006; Hartman et al. 2009). The modern 0.5%–1% occurrence rate suggests that these early transit surveys would have needed a greater data volume at higher precision for detection to be possible (Mayor et al. 2011; Howard et al. 2012; Wright et al. 2012; Petigura et al. 2018).

Kepler observed a large enough number of stars with a sufficient baseline and precision to detect transiting planets in open clusters: Kepler-66b and 67b, in the gigayear-old NGC 6811 (Borucki et al. 2010; Meibom et al. 2013). Though a broken reaction wheel ended the prime Kepler mission, the repurposed K2 (Howell et al. 2014) switched between fields along the ecliptic every quarter-year and was able to observe far more clusters and young stars.

The discoveries made by K2 through its surveys of Taurus, the Hyades, Praesepe, and Upper Sco were a major inspiration for the present work (e.g., Mann et al. 2016a, 2017, 2018; Obermeier et al. 2016; Ciardi et al. 2018; Livingston et al. 2018, 2019; Rizzuto et al. 2018; Vanderburg et al. 2018). Observations with K2 convincingly showed that at least some close-in planets must form within about 10 Myr (David et al. 2016; Mann et al. 2016b). They also led to the first hints that young planets in clusters may in fact be qualitatively different from their field counterparts. For instance, based on its observed mass, radius, and UV environment, the 700 Myr K2-100b is probably actively losing its atmosphere and should become a bare rocky planet over the next few hundred megayears (Mann et al. 2017; Barragán et al. 2019). The four transiting planets around V1298 Tau (23 Myr) are also likely to be photoevaporating and could represent a precursor to Kepler’s compact multiple systems (David et al. 2019a, 2019b).

To advance the young-planet census, we have been using data from the Transiting Exoplanet Survey Satellite (TESS; Ricker et al. 2015) to perform a Cluster Difference Imaging Photometric Survey (CDIPS; Bouma et al. 2019). Our targets in this survey are candidate young stars that have been reported in the literature. At the time of writing,  $\sim 6 \times 10^5$  light curves from Year 1 of TESS have been created and made available through the Mikulski Archive for Space Telescopes<sup>28</sup> (MAST) and via [10.17909/t9-ayd0-k727](https://doi.org/10.17909/t9-ayd0-k727). Searching through a subset of these light curves brought our attention to the candidate transiting planet TOI 837b, which is the subject of this analysis.

The transits of TOI 837b are grazing the stellar limb, which is a cause for concern. Particularly for a star near the galactic

<sup>28</sup> [archive.stsci.edu/hlsp/cdips](https://archive.stsci.edu/hlsp/cdips)

plane ( $b = -5.8$ ), background eclipsing binaries are a major source of astrophysical false positives (e.g., Sullivan et al. 2015, Figure 30). Our follow-up data showed that this and related scenarios are unlikely to the degree that we could validate the planet, i.e., determine that its probability of being an astrophysical false positive is small. We considered this result worth reporting because of the planet’s youth.

Section 2 describes the identification of the candidate and our follow-up observations. Section 3 combines the available data to assess the system’s false-positive probability (FPP) and validates TOI 837b as a planet. Section 4 presents our knowledge of the cluster (Section 4.1), the star (Section 4.2), and the planet (Section 4.3). We conclude by discussing avenues for confirmation and improved characterization in Section 5.

## 2. Identification and Follow-up Observations

### 2.1. TESS Photometry

TOI 837 was observed by TESS from 2019 March 26 to 2019 May 20, during Sector 10 and Sector 11 of its science operations (Ricker et al. 2015). The star was designated TIC 460205581 in the TESS Input Catalog (Stassun et al. 2018, 2019). Pixel data for an  $11 \times 11$  array surrounding the star were co-added and saved at a 2 minute cadence. A  $2048 \times 2048$  image from the entire charge-coupled device (CCD) was also co-added into 30 minute stacks and saved as a “full-frame image” (FFI).

The TESS Science Processing Operations Center (SPOC; Jenkins et al. 2016) processed the image data and identified the transiting-planet signature from two transits in Sector 10, again with three transits in Sector 11, and for a final time when Sectors 1–13 were searched at the end of the first year of the mission. The transit signature was fitted with a limb-darkened transit model (Li et al. 2019) and passed all the diagnostic tests (Twicken et al. 2018), including the odd/even depth test, the weak secondary-eclipse test, and the difference image centering test, which placed the transit source within  $\sim 2''$  of the location of TOI 837. No additional transit-like features were identified in any of the SPOC searches. The TESS Science Office alerted the community to this candidate transiting planet on 2019 June 17. Our subsequent blind search of the CDIPS FFI light curves also showed the transits, as did that of Nardiello et al. (2020). Given that the 2 minute data had better sampling cadence, we opted to use the Presearch Data Conditioning light curve with the default aperture for our analysis (Smith et al. 2012, 2016; Stumpe et al. 2014).

The top panel of Figure 1 shows the TESS data. The dominant modulation induced by starspots coming into and out of view has a peak-to-peak amplitude of about 2.3% and a period of about 3 days. The dips are suggestive of a grazing transiting planet, recurring roughly every 8 days with a depth of about 0.4%. A few flares are also visible. A phase-folded view of the TESS transits combined with ground-based follow-up photometry is shown in the bottom panel of Figure 1. The ground-based data and our fitting procedure are discussed in Sections 2.4 and 4.3, respectively. First though, some prerequisite context on the stellar neighborhood of TOI 837 is needed.

### 2.2. Gaia Astrometry and Imaging

Between 2014 July 25 and 2016 May 23, the European Space Agency’s Gaia satellite measured about 300 billion centroid positions of 1.6 billion stars. The positions, proper motions, and parallaxes of the brightest 1.3 billion were calculated for the second data release (DR2; Gaia Collaboration et al. 2016, 2018; Lindegren et al. 2018). TOI 837 was assigned the Gaia DR2 identifier 5251470948229949568 and had 276 “good” astrometric observations. Its brightness was measured in the  $G$ ,  $R_p$ , and  $B_p$  bands of the Radial Velocity Spectrometer (Cropper et al. 2018; Evans et al. 2018).

The Gaia imaging, reduced to its point-source catalog, provides the initial context for analyzing the TESS data. Stars brighter than  $T = 16$ , as queried from the Gaia DR2 source catalog, are shown with white circles in Figure 2, overlaid on the TESS image. Given its galactic latitude of  $b = -6^\circ$ , it is not surprising that the field of TOI 837 is crowded. The resolved stars that were of immediate concern for our false-positive analysis were as follows.

1. TOI 837  $\equiv$  TIC 460205581 ( $T = 9.9$ ). The target star.
2. Star A  $\equiv$  TIC 847769574 ( $T = 14.6$ ),  $2''_3$  west. The proper motions and parallax of this star imply that it is co-moving with TOI 837 and that the two stars are separated by  $6.6 \pm 0.1$  pc. Star A is therefore likely to be an IC 2602 member but unlikely to be a bound binary companion.
3. Star B  $\equiv$  TIC 460205587 ( $T = 13.1$ ),  $5''_4$  north. The Gaia parallax implies this is a background giant star.

An additional source, TIC 847769581, is located  $4''_9$  from the target but is too faint ( $T = 18.8$ ) to be the source of the observed transit signal.

The Gaia DR2 data for Star A seem poorly behaved. While Star A has  $G = 15.1$  and  $B_p = 14.9$ , no  $R_p$  magnitude is reported. Correspondingly, no renormalized unit weight error (RUWE)<sup>29</sup> value is available. We suspect that the photometric failure to produce an  $R_p$  magnitude and the poor astrometric fit of this star are due to blending with TOI 837.

At the  $\approx 1'$  resolution of the TESS data, if either Star A or Star B was an eclipsing binary, it could be the source of the transit signal. A detailed analysis of ground-based seeing-limited photometry was necessary to assess and rule out this possibility (Section 2.4 and Figure 4).

### 2.3. High-resolution Imaging

To determine if any fainter point sources existed closer to TOI 837 inside of Gaia’s point-source detection limits, we acquired high-resolution speckle images. We then searched the autocorrelation functions of these images for peaks indicative of nearby companions.

Observations of TOI 837 were initially acquired by Ziegler et al. (2020) as part of the Southern Astrophysical Research (SOAR) TESS Survey using the High Resolution Camera (HRCam; Tokovinin 2018). The HRCam  $I$ -band filter has been described by Tokovinin (2018). The points in Figure 3 show the resulting measured  $5\sigma$  detectable contrasts. The lines are linear smoothing fits between the regimes of the diffraction limit, the “knee” at  $\approx 0''_2$ , and the slow decrease until  $\approx 1''_5$ ,

<sup>29</sup> See the Gaia Data Processing and Analysis Consortium technical note GAIA-C3-TN-LU-LL-124-01, [http://www.rssd.esa.int/doc\\_fetch.php?id=3757412](http://www.rssd.esa.int/doc_fetch.php?id=3757412), 2020-07-08.

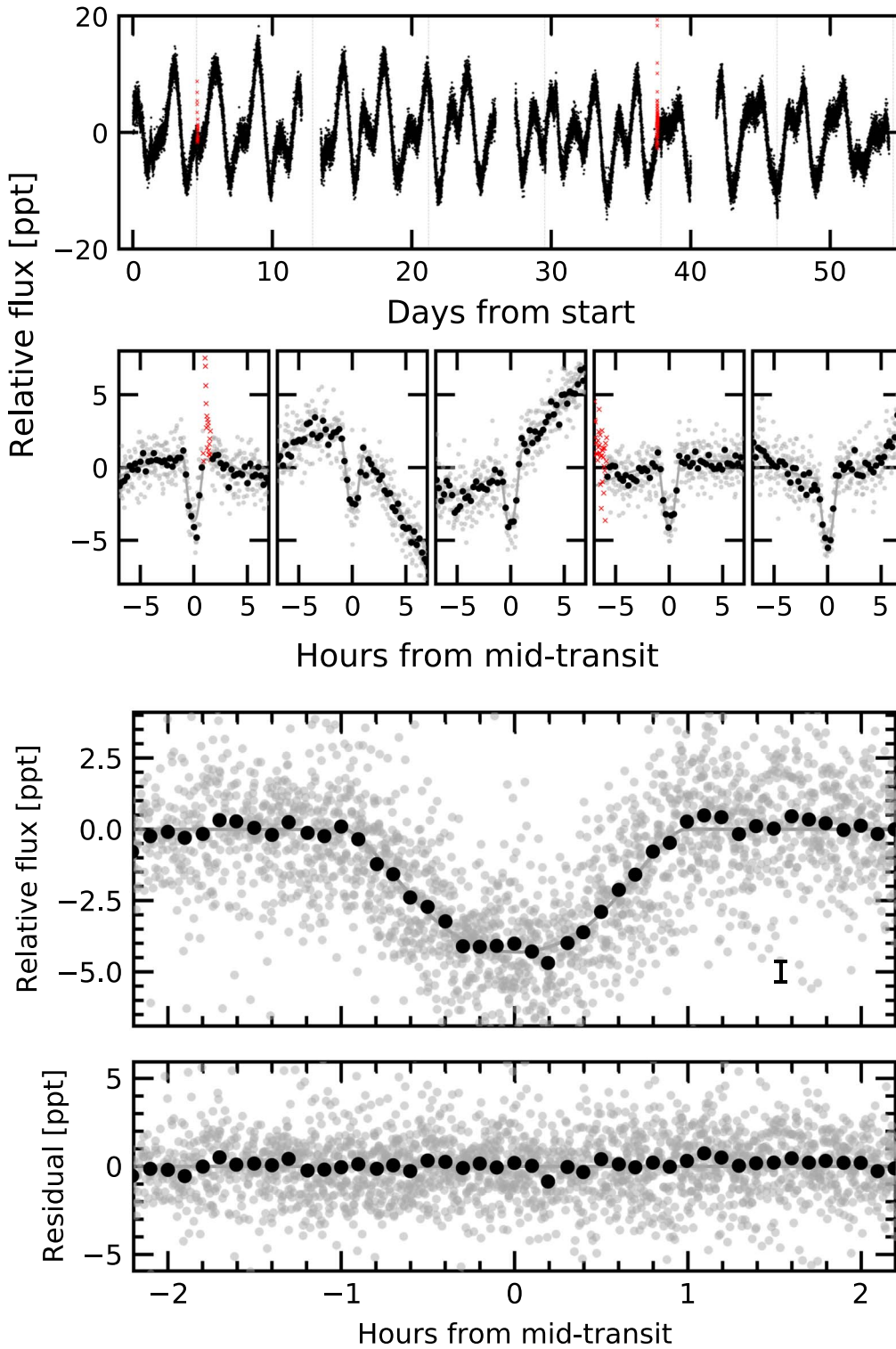


**Figure 1.** Light curves of TOI 837. Top: TESS PDCSAP median-subtracted relative flux at 2 minute sampling in units of parts per thousand ( $\times 10^{-3}$ ). Starspot-induced variability is the dominant signal; flares are shown with red crosses. Dashed lines indicate the five transits observed by TESS over Sectors 10 and 11. Middle: Individual TESS transits. The gray lines are the best-fit model to the TESS and ground-based data, which includes a local quadratic trend for each transit. The gray points are 2 minute PDCSAP flux measurements, and the black points are binned to 15 minute intervals. Bottom: Phase-folded TESS and ground-based transits. Section 2.4 presents the ground-based data. The gray points are flux measurements with the local spot-induced variation removed. A weighted binning at 6 minute intervals yields the black points. The black error bar shows the median uncertainty for the black points. The gray line is the best-fit model for the entire data set.

beyond which the speckle patterns become decorrelated. Star A (TIC 847769574) was detected at the expected location and brightness contrast, and no additional companions were found. Star B was not detected; with a separation of  $5''.4$  from TOI 837, it fell outside the field of view.

#### 2.4. Ground-based Time-series Photometric Follow-up

We obtained ground-based seeing-limited time-series photometric observations of TOI 837 bracketed around the times of transit. These observations confirmed that the transits occurred

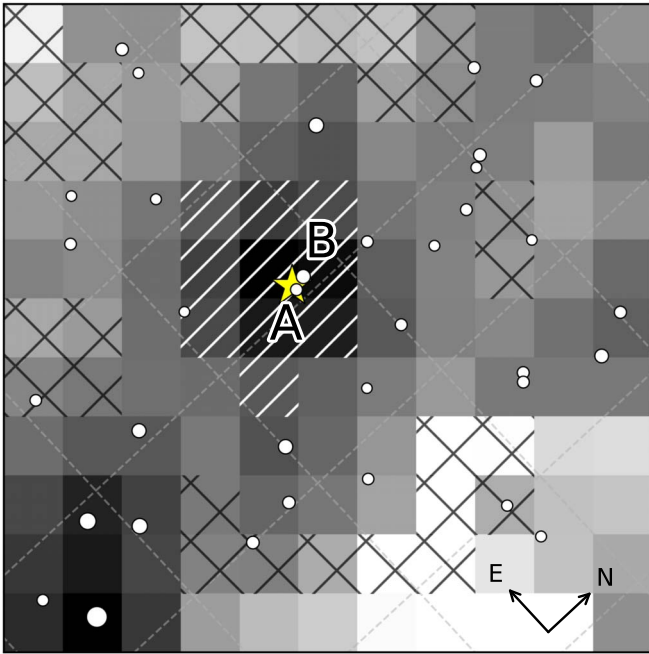


**Figure 2.** Scene of TOI 837. Mean TESS image of TOI 837 from Sector 10 on an  $11 \times 11$  pixel cutout, with a logarithmic grayscale indicating the flux in each pixel. The yellow star is the position of TOI 837. The white circles are resolved Gaia sources with  $T < 16$ , with larger ones indicating brighter stars. The black crosses and white hatches show the apertures used to measure the background and target star flux, respectively. The compass shows the cardinal directions in celestial coordinates. The dashed lines of constant decl. are separated by  $1'$ , while those of R.A. are separated by  $2'$ . The two stars of interest are “Star A” and “Star B,” which were excluded as possible sources of the transits.

on target to within  $\approx 2''$  and that they were achromatic. Both features are essential for our ability to eliminate false-positive scenarios.

#### 2.4.1. El Sauce 0.36 m

*Acquisition and reduction*—We observed four transits with the 0.36 m telescope at Observatorio El Sauce, located in the Río Hurtado Valley in Chile and operated by coauthor P. Evans. The observations were obtained in the Cousins-*R* band on the nights of 2020 April 1 and 26, the Cousins-*I* band on the night of 2020 May 21, and the Johnson-*B* band on the night of 2020 June 14. The final June 14 transit began shortly after twilight.

We scheduled our transit observations using the TESS Transit Finder, which is a customized version of the Tapir software package (Jensen 2013). The photometric data were calibrated and extracted using AstroImageJ (Collins et al. 2017). Comparison stars of similar brightness were used to produce the final light curves, each of which showed a roughly 4 ppt dip near the expected transit time. The data are reported in Table 1 and plotted in Figure 4.

*Custom aperture analysis*—Based solely on the TESS data, both Star A and Star B were possible sources of blended eclipsing binary signals. The typical FWHM for stars in the El Sauce observations was  $\approx 2''/3$ , with a variance of  $\approx 0''/2$ . Star B is resolved in the 0.36 m images; Star A is not.

To rule out blend scenarios with the ground-based photometry, we produced light curves centered on TOI 837 with circular apertures of radii ranging from  $0''/7$  to  $5''/1$ . We did not

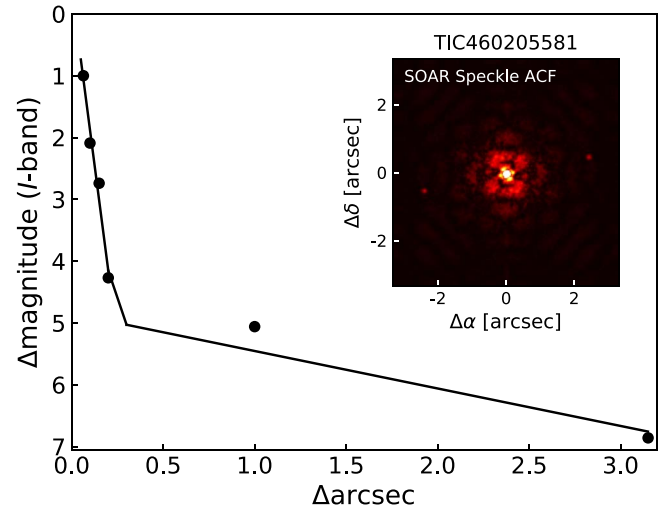


**Figure 3.** Speckle imaging of TOI 837. Contrast limits from SOAR HRCam imaging were derived from point-source injection–recovery experiments. Star A ( $\Delta T = 4''/7$ ,  $2''/3$  west) is detected and is also a resolved Gaia source. It is co-moving with TOI 837, and its parallax and on-sky position imply that it is physically separated from TOI 837 by  $6.6 \pm 0.1$  pc.

**Table 1**  
Ground-based TOI 837 Photometry

Time [BTJD <sub>TDB</sub> ]	Rel. Flux	Rel. Flux Err.	Instrument
1940.487018	0.999998	0.002430	El Sauce
1998.700107	0.998675	0.001621	ASTEP

**Note.** Table 1 is published in its entirety in a machine-readable format. Two example entries are shown for guidance regarding form and content. To convert from the Barycentric TESS Julian Date to the Barycentric Julian Date, add 2,457,000. See Eastman et al. (2010) for descriptions of the barycentric and leap-second corrections.

(This table is available in its entirety in machine-readable form.)

detect any statistically significant variation in the depth of the transits with aperture size. Beyond the difference image centroiding test performed by the SPOC pipeline, two additional lines of evidence ruled out Star B as the eclipsing source: first, the transits were detected in the smallest apertures. Second, we made light curves with  $2''/1$  apertures centered on Star B, and they did not show the transit.

To assess the possibility that Star A is an eclipsing body, we created light curves with a custom set of circular apertures with radii of  $2''/1$  and positions ranging from Star A ( $2''/3$  west of TOI 837) to  $2''/3$  east of TOI 837. We did not detect any variation of the transit depth along this line of light curves. The apertures east of TOI 837 excluded over 90% of the flux from Star A. The eclipse on Star A would therefore need to have depth greater than unity to produce the observed eclipse depth. We therefore interpret the lack of asymmetry between the westernmost (centered on Star A) and easternmost (furthest from Star A) light curves as conclusive evidence that TOI 837 is the source of the transit signal to within  $\approx 2''/0$ . To verify self-consistency, we checked that the maximum dilution from Star A ( $\approx 1\%$ ) is less than the uncertainty of the transit depth measurements ( $\approx 15\%$ ), and so the lack of variation of transit depth with aperture location is consistent with TOI 837 being the source of transits.

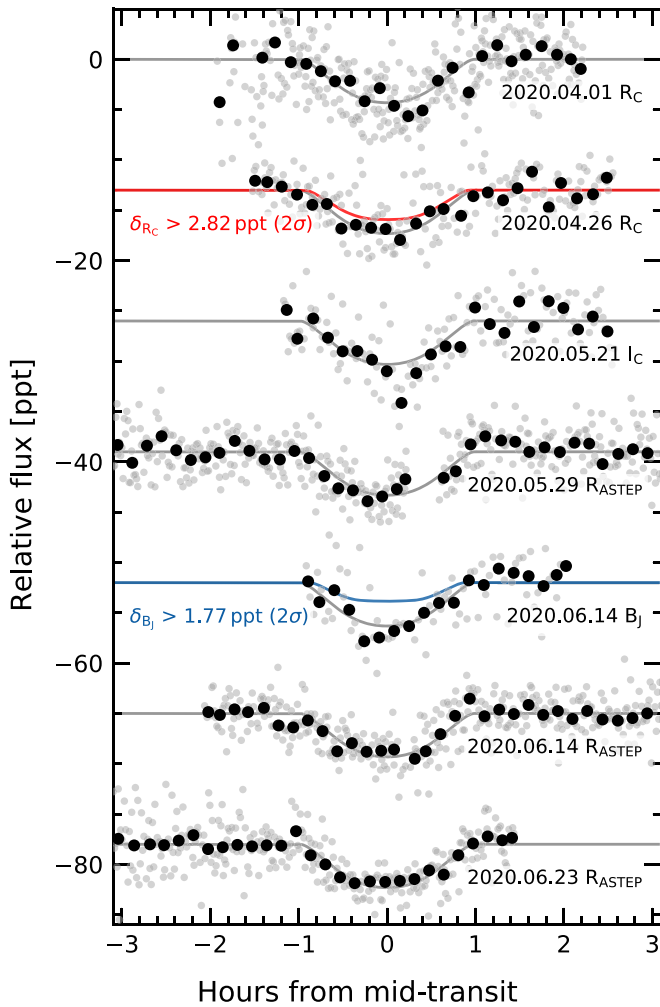


**Figure 4.** Ground-based follow-up photometry. The data were acquired using the 0.36 m telescope at El Sauce and the 0.40 m ASTEP400 telescope at Dome C. Black points represent the measurements after binning at 10 minute intervals. The gray line is the model that best fits the combined TESS and ground-based data. Red and blue lines show  $2\sigma$  lower limits on the transit depths in the Cousins- $R$  and Johnson- $B$  bandpasses used to rule out specific false-positive scenarios (see Section 3.1.5).

An additional line of evidence for Star A not being the transit host was also noted by the referee. The  $G$ -band magnitude and the parallax suggest that Star A is an M dwarf. As a probable cluster member, it would have  $B_p - R_p \approx 2.8$  (see Section 4.1.2), which corresponds roughly to a mass in the range of  $0.15\text{--}0.45 M_\odot$ , or to densities roughly in the range of  $2\text{--}3 \text{ g cm}^{-3}$  based on the Padova-Trieste Stellar Evolution Code (PARSEC) isochrones (Bressan et al. 2012; Chen et al. 2014, 2015; Marigo et al. 2017). These densities are inconsistent with those inferred from the transit fits in Section 4.3.

#### 2.4.2. ASTEP400

We observed three transits with the 0.40 m Antarctic Search for Transiting Exoplanets (ASTEP) telescope at the Concordia base on the Antarctic Plateau (Daban et al. 2010). The Concordia base is operated by the French and Italian polar institutes, IPEV and PNRA. Its position on the Antarctic

Plateau allows it to take advantage of the continuous night during austral winter. The weather is of photometric quality for about two-thirds of each winter (Crouzet et al. 2018).

ASTEP is equipped with an FLI ProLine science camera with a KAF-16801E,  $4096 \times 4096$  front-illuminated CCD. The camera has an image scale of  $0''.93 \text{ pixel}^{-1}$ , resulting in a  $1^\circ \times 1^\circ$  corrected field of view. The focal instrument’s dichroic plate splits the beam into a blue wavelength channel for guiding and a non-filtered red science channel roughly matching a Cousins- $R$  transmission curve (Abe et al. 2013; Mékarnia et al. 2016). The images were processed on site using an automated aperture photometry pipeline based on the daophot package of the IDL Astronomy User’s Library (Landsman 1995).

TOI 837 was observed with ASTEP on 2020 May 12, May 29, June 14, and June 23 (Universal Time). Except for May 12, our observations were conducted under stable weather conditions, with clear skies, temperatures of about  $-70^\circ\text{C}$ , and wind speeds less than  $5 \text{ m s}^{-1}$ . Due to their poor quality, we excluded from the analysis all data collected on May 12. We found that the optimal calibrated light curves of TOI 837 correspond to an 11 pixel ( $10''$ ) and 14 pixel ( $12''$ ) radius aperture for the observations carried out on June and May, respectively. The data are reported in Table 1 and plotted in Figure 4.

#### 2.5. Spectroscopic Follow-up

Reconnaissance spectroscopic follow-up is an essential step in vetting planet candidates. Medium- to high-resolution spectra enable physical characterization of the star and therefore the planet. Reducing multiple spectra to RVs can enable planet mass measurements and can also lead to limits on the mass of nearby companions. Finally, if there are close or bright companions, reconnaissance spectra can also reveal the presence of a secondary set of stellar lines.

##### 2.5.1. SMARTS 1.5 m/CHIRON

We acquired nine spectra using CHIRON at the SMARTS 1.5 m telescope at the Cerro Tololo Inter-American Observatory (CTIO), Chile (Tokovinin et al. 2013). Six met our signal-to-noise requirements for RV measurements and stellar parameter extraction. We used CHIRON in its image slicer configuration, yielding a spectral resolution of  $\approx 79,000$  across  $415\text{--}880 \text{ nm}$ .

We derived RVs and spectroscopic line profiles from the CHIRON observations using a least-squares deconvolution (LSD) of the spectra against nonrotating synthetic spectral templates (Donati et al. 1997). The spectral templates were generated using ATLAS9 atmosphere models (Castelli & Kurucz 2004) with the SPECTRUM script (Gray & Corbally 1994). These line profiles were fitted with a broadening kernel that describes the rotational, radial-tangential macroturbulent, and instrumental broadening of the spectrum. The rotational and macroturbulent broadening were computed as per Gray (2005), following the methods described in Zhou et al. (2018). We fitted the line profile from each observation independently, yielding the RVs listed in Table 2 and shown in Figure 5. We found a mean rotational broadening velocity of  $v \sin i_* = 16.2 \pm 1.1 \text{ km s}^{-1}$  and a macroturbulent broadening of  $v_{\text{mac}} = 8.4 \pm 2.9 \text{ km s}^{-1}$ .

**Table 2**  
TOI 837 RVs

Time [BJD <sub>TDB</sub> ]	RV (m s <sup>-1</sup> )	$\sigma_{RV}$ (m s <sup>-1</sup> )	Instrument
8669.533150	-57.8	27.5	FEROS
8669.540450	-13.9	29.4	FEROS
8676.506930	6.7	37.8	FEROS
8677.519150	-70.3	44.6	FEROS
8884.787630	240.0	28.0	CHIRON
8891.891180	-76.0	37.0	CHIRON
8898.735330	-10.0	43.0	CHIRON
8903.725760	-25.0	38.0	CHIRON
8904.739930	80.1	24.5	FEROS
8905.793630	88.0	21.7	FEROS
8908.762520	45.3	28.3	FEROS
8909.702140	0.0	31.8	FEROS
8912.606750	41.3	24.1	FEROS
8913.740580	161.1	37.3	FEROS
8915.762170	10.0	33.0	CHIRON
8916.714540	-93.5	33.6	FEROS
8917.765720	-159.7	24.8	FEROS
8920.706100	99.0	32.0	CHIRON
8922.845800	-148.3	54.9	FEROS
8915.924027	37.5	725.9	Veloce
8921.284950	105.9	453.2	Veloce
8922.733572	-195.9	195.6	Veloce
8924.583708	-7.6	262.3	Veloce
8926.365810	14.3	442.6	Veloce
8927.318146	207.0	505.2	Veloce
8928.559780	-7.3	180.2	Veloce
8930.324059	-2.6	152.0	Veloce
8931.293091	-45.7	152.9	Veloce
8932.065206	-105.6	319.8	Veloce

**Note.** Times are in units of BJD<sub>TDB</sub>-2,450,000.

To derive the stellar parameters, we matched the set of CHIRON spectra against a library of observed spectra, previously obtained using the Tillinghast Reflector Echelle Spectrograph (Fűrész et al. 2008) on the 1.5 m reflector at the Fred Lawrence Whipple Observatory, Arizona, USA, and classified using the Stellar Parameter Classification pipeline (Buchhave et al. 2010). We found the best-matching stellar parameters to be  $T_{\text{eff}} = 5899 \pm 55$  K,  $\log g = 4.496 \pm 0.011$  dex, and  $[\text{Fe}/\text{H}] = -0.069 \pm 0.042$  dex. We ultimately adopted a different set of stellar parameters for our analysis (see Section 4.2.4).

The spectroscopic line profiles were thoroughly examined for any signs of secondary lines that might indicate the presence of another star, either associated or in chance alignment with TOI 837. No such set of lines was found. To set limits on the contributions of a close-by star to the observed spectrum, we injected a secondary signal into the mean LSD profile derived from the CHIRON observations. The injection spanned 10,000 different combinations of line broadening, velocity separation, and flux ratio  $F_2/F_1$ . The recovery results showed that for rotational broadenings of the secondary of 5, 15, and 25 km s<sup>-1</sup>, we were able to exclude sources with flux fractions  $F_2/F_1$  brighter than roughly 0.03, 0.08, and 0.20, provided that the secondary was separated from the primary by at least  $\approx 15$  km s<sup>-1</sup>. At smaller velocity separations, the injected lines began to blend with the target spectrum. We verified these results by injecting secondary lines directly into the spectrum and then deriving their LSD broadening profile as

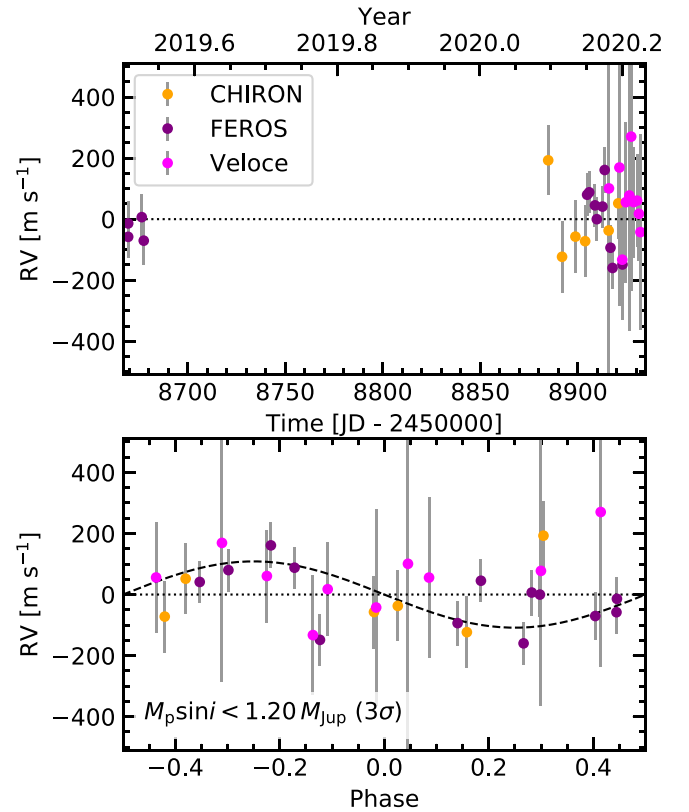


**Figure 5.** Velocimetry of TOI 837. Top: RV measurements, with best-fit instrument offsets and jitter terms included. The expected scatter from starspots based on  $v \sin i$  and the photometric modulation amplitude is  $\sim 300$  m s<sup>-1</sup>. Bottom: RV measurements phased to the orbital ephemeris of TOI 837b. The planet is not detected. The dashed black line shows a circular Keplerian orbit representing the  $3\sigma$  upper mass limit.

we would for a normal observation. The results were nearly identical, save for greater computational cost.

### 2.5.2. FEROS

TOI 837b was monitored with the FEROS echelle spectrograph (Kaufer et al. 1999), mounted on the MPG 2.2 m telescope at the European Southern Observatory’s (ESO) La Silla Observatory in Chile. FEROS has a resolution of  $\approx 48,000$  across a spectral range of 350–920 nm. It has a high efficiency of  $\approx 20\%$ . We obtained 13 spectra of TOI 837 between 2019 July 5 and 2020 March 14 in the context of the Warm Giants with TESS collaboration, which focuses on the systematic characterization of TESS transiting giant planets with moderately long orbital periods (e.g., Brahm et al. 2019; Jordán et al. 2020). We adopted exposure times of 500 and 600 s, and the observations were performed with the simultaneous calibration mode for tracing the instrumental velocity variations with a comparison fiber illuminated with a ThAr lamp. FEROS data were processed with the *ceres* pipeline (Brahm et al. 2017), which delivers precision RVs and bisector span measurements through cross-correlation of the extracted spectra with a binary mask resembling the properties of a G2V star. The RVs are given in Table 2 and shown in Figure 5. To check for the presence of secondary lines, we performed an injection–recovery exercise similar to that with the CHIRON data. We achieved slightly worse limits, likely due to the lower spectral resolution of FEROS, and therefore adopted the CHIRON limits.

### 2.5.3. *Veloce*

We acquired 34 spectra over 10 visits of TOI 837 using the *Veloce* spectrograph, mounted on the 3.9 m Anglo-Australian Telescope (AAT) at Siding Spring Observatory near Coonabarabran, Australia (Gilbert et al. 2018). The currently operational “*Veloce Rosso*” channel provides coverage from 600 to 950 nm at a spectral resolution of  $\approx 80,000$ . Many of the exposures were taken in average or poor seeing conditions, when the signal-to-noise ratio (S/N) was lowest and the fiber-to-fiber cross-contamination on the integral field unit-style fiber feed was strongest. To reduce the spectra to velocities, we cross-correlated against a template of  $\delta$  Pavonis, because with spectral type G8 IV it was the closest high-S/N TOI 837 analog available in the *Veloce* spectral database. The velocity rms seen across each visit was hundreds of meters per second, likely due to uncorrected fiber-to-fiber cross-contamination. This cross-contamination severely affected the wavelength solutions for the 19 individual science fibers, ultimately leading to significantly increased RV scatter. For analysis purposes, we averaged the single-shot RVs across each visit and set the velocity uncertainties to be the standard deviation of the per-visit exposures. The velocities are given in Table 2 and shown in Figure 5.

## 3. Assessment of False-positive Scenarios

Validating a transiting planet means statistically arguing that the data are much more likely to be explained by a planet than by an astrophysical false positive. The concept of validation has been developed and calibrated by, e.g., Torres et al. (2011), Morton (2012), Díaz et al. (2014), Santerne et al. (2015), Morton et al. (2016), and Giacalone & Dressing (2020). “Validation” is different from “confirmation,” which means that there is overwhelming evidence that the transits must be explained by a planet, through elimination of all false-positive scenarios and determination that the planet’s mass is in the substellar regime.

Assuming an eclipse has been localized to the target star, potential false-positive scenarios include eclipses of an unresolved background binary (BEB), eclipses of a hierarchical system bound to the primary star (HEB), and the possibility that the eclipses are caused by a stellar companion rather than a planetary one (EB).

Figure 6 provides a visual summary of the possible astrophysical false-positive scenarios, as well as our ability to rule them out based on our combined photometry, velocimetry, and imaging. In this section we describe each constraint in turn and then present a calculation using *VESPA* (Morton 2012) to demonstrate that the probability of TOI 837 being an astrophysical false positive is small enough to validate it as a planet.

### 3.1. Constraints on False-positive Scenarios

#### 3.1.1. Transit Depth

In HEB and BEB scenarios, the flux from TOI 837 and the true eclipsing binary host blend together and reduce the “true” TESS-band eclipse depth  $\delta_{\text{true}}$  to the observed depth  $\delta_{\text{obs}}$ :

$$\delta_{\text{obs}} = \delta_{\text{true}} \frac{F_{\text{comp}}}{F_{\text{total}}}, \quad (1)$$

where the total system flux and the flux from only the companion binary are labeled as such. The requirement that the eclipse is produced by fusion-powered stars and that  $\delta_{\text{true}} < 0.5$

translates to a bound on the faintest possible blended companion system:

$$\Delta m < -\frac{5}{2} \log_{10} \left( \frac{0.5}{\delta_{\text{obs}}} \right). \quad (2)$$

For TOI 837 ( $T = 9.93$ ), this implies that any stellar companion invoked to explain the transit depth must be brighter than  $T = 15.07$ . In Figure 6, we set the spatial limit to  $2''$  based on the precision at which we have localized the transits using seeing-limited ground-based photometry.

If the transit were box-shaped, this argument could be extended to even more restrictive depths (e.g., Seager & Mallén-Ornelas 2003; Vanderburg et al. 2019; Rizzuto et al. 2020). Since the transits of TOI 837 could be grazing, the second and third contact points do not necessarily occur, and the shape of the transit is not particularly restrictive.

#### 3.1.2. Speckle Imaging

The contrast limits obtained through the SOAR *I*-band speckle imaging (Section 2.3) are shown in Figure 6. While “Star A” was detected in the SOAR images, our ground-based photometry rules it out as a possible source of the eclipse signal (Section 2.4). To convert the remaining contrast constraints to limits on the masses of bound companions, we used the Baraffe et al. (2003) models for substellar-mass objects and the MESA Isochrones and Stellar Tracks (MIST) models for stellar-mass objects (Paxton et al. 2011, 2013, 2015; Choi et al. 2016; Dotter 2016). We assumed that the system age was 35 Myr, so that companions would be at a plausible state of contraction.

To convert from theoretical effective temperatures and bolometric luminosities to expected magnitudes in instrumental bandpasses, we made the simplifying assumption that all sources had blackbody spectra. Using the theoretical stellar parameters and the measured transmission functions (Tokovinin 2018), we then calculated the apparent magnitudes of stellar companions of different masses and interpolated to produce the scale shown on the upper right in Figure 6.

#### 3.1.3. Not SB2

We derived limits on blended spectroscopic companions using the stacked CHIRON spectra (see Section 2.5.1). For a slowly rotating stellar companion well separated in velocity, the spectra would have revealed companions with flux fractions  $F_2/F_1 \gtrsim 3\%$ . For a companion with rotational broadening of  $15 \text{ km s}^{-1}$ , roughly equivalent to that of TOI 837, we were able to exclude companions with flux fractions exceeding  $\approx 8\%$ . For plotting purposes, in Figure 6 we assume the latter flux-fraction limit of  $8\%$  ( $\Delta \text{mag} \approx 2.7$ ). The outer limit in projected separation for associated companions is the distance at which the Keplerian orbital velocity is well below the rotational broadening. This condition translates to a projected separation of 10–20 au, depending on the companion mass. For chance alignments, the same restrictions on velocity separation apply, but out to a projected separation equal to the CHIRON slit width of  $\approx 1''$ .

#### 3.1.4. RVs

The RVs from FEROS, CHIRON, and *Veloce* can be used to detect massive bound companions orbiting TOI 837. We searched for planetary- and stellar-mass companions in two

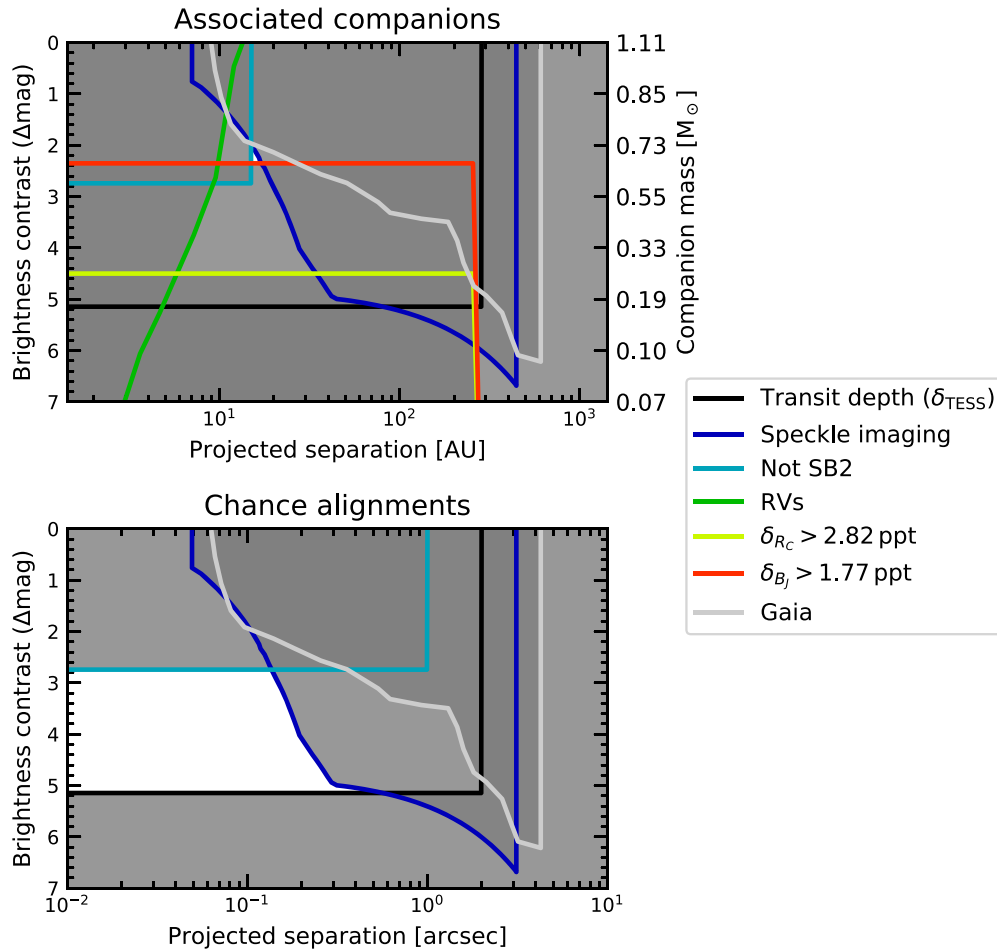


**Figure 6.** Astrophysical false-positive scenarios. Top: For bound companions (EB and HEB scenarios). Bottom: For unassociated companions along the same line of sight (BEB scenarios). Each constraint is described in Section 3.1. Gray regions are ruled out by at least one constraint.

different regimes: first at the orbital period of the transiting object and second at longer orbital periods to constrain the presence of a massive bound companion.

For the first fit we set a prior on the period and time of conjunction using the known ephemeris from the transit. We then fitted for the semi-amplitude, instrument offsets, and jitter parameters using `radvel` (Fulton et al. 2018) and assuming circular orbits. This yielded a nondetection of the planet’s orbit. The corresponding  $3\sigma$  (99.7th percentile) upper limit on  $M_p \sin i$  is  $1.20 M_{\text{Jup}}$ . The data and corresponding model are shown in Figure 5.

The above exercise ruled out the possibility that the observed eclipses were caused by a stellar-mass object orbiting TOI 837. The lack of a linear RV trend, particularly in the FEROS data, further constrains the presence of a hierarchical binary system. Fitting a line to the FEROS velocities yielded a  $3\sigma$  limit on linear RV trends of  $|\dot{\gamma}| < 0.82 \text{ m s}^{-1} \text{ day}^{-1}$ , over the 253 day FEROS baseline. The agreement between the mean Gaia DR2 velocity ( $17.44 \pm 0.64 \text{ km s}^{-1}$ ) and that from FEROS ( $18.0 \pm 0.1 \text{ km s}^{-1}$ ) in theory places an additional limit on linear trends, since the two observation epochs are separated by roughly 5 years.

To place limits on the properties of a possible bound hierarchical companion, we performed the following injection–recovery exercise. We simulated  $10^6$  two-body systems with random orbital phases and inclinations and drew their semi-amplitudes

and periods from logarithmic distributions:  $K \text{ [m s}^{-1}] \sim \log \mathcal{U}(1, 10^7)$  and  $P \text{ [days]} \sim \log \mathcal{U}(1, 10^{15})$ . Again assuming circular orbits, we then analytically evaluated what the RVs would have been at the observed FEROS times if the system had the assumed parameters. We then calculated what the linear slope would have been for each simulated system. If the absolute value of the slope exceeded our  $3\sigma$  limit of  $|\dot{\gamma}| < 0.82 \text{ m s}^{-1} \text{ day}^{-1}$ , we assumed that we would have detected such a system. Figure 6 shows the resulting limits; weakened sensitivity at harmonics of the baseline occurred at lower masses and smaller projected separations than shown on the plot. The interpolation from mass to brightness contrast was performed using the same isochrone models and assumptions in Section 3.1.2.

### 3.1.5. Multicolor Photometry

*Multicolor photometry and HEB scenarios*—The most plausible HEB scenarios for TOI 837 involve pairs of eclipsing M dwarfs (Figure 6). Eclipses of such stars are much redder than eclipses of the G dwarf TOI 837. Limits on whether the transit depth decreases in bluer bandpasses can therefore rule out certain HEB scenarios.

We fitted the observed depths in different bandpasses using machinery similar to that described in Section 4.3. We fitted each ground-based transit individually for the planet-to-star size ratio, the impact parameter, and a local quadratic trend (the ephemeris was assumed from an initial fit of only the

TESS data). The corresponding  $2\sigma$  lower limits on the transit depths in Cousins- $R$  and Johnson- $B$  band light curves were 2.82 and 1.77 ppt, respectively, and are shown in Figure 4. Particularly in our Johnson- $B$  light curve, the transit depth is correlated with the mean and linear slope of the light curve: a smaller depth is allowed if the data are fitted with a larger linear slope and a larger mean. Our quoted limits marginalize over these correlations, and the depth measurement itself is nearly Gaussian.

To determine what classes of HEB are eliminated by these limits, we performed the following calculation. We assumed that each system was composed of the primary (TOI 837), plus a tertiary companion eclipsing a secondary companion every 8.3 days. For secondary masses ranging from 0.07 to  $1.10 M_{\odot}$  and mass ratios ( $M_3/M_2$ ) ranging from 0.1 to 1, we then calculated the observed maximal eclipse depth caused by Star 3 eclipsing Star 2 in each observed bandpass. As before, we interpolated between mass, effective temperature, and radius assuming the MIST isochrones for a 35 Myr old system and also assumed that each source had a blackbody spectrum. We used the transmission functions from the Spanish Virtual Observatory (SVO) Filter Profile Service.<sup>30</sup> For a typical HEB system (e.g.,  $M_2 = M_3 = 0.2 M_{\odot}$ ), the bluest optical bandpasses produced eclipses with roughly a tenth of the depth of those in the TESS band, because the M-dwarf blackbody function turns over at much redder wavelengths than the G-dwarf blackbody (Wien’s law).

For a fixed secondary mass, we then asked whether any tertiary companions existed for which the maximal expected eclipse depth could have been larger than the observed depth. We could not rule out hierarchical eclipsing binary systems in cases for which the answer was yes. Conversely, we ruled out systems for which at fixed secondary mass no tertiary mass could enable eclipses of the necessary depth (in the  $R_C$  band or  $B_J$  band). The  $R_C$ -band limit corresponded to a secondary-mass limit of  $M_2 > 0.27 M_{\odot}$ , and the  $B_J$ -band limit corresponded to a stronger limit of  $M_2 > 0.70 M_{\odot}$ .

*Multicolor photometry and BEB scenarios*—While the above constraints rule out HEBs, certain configurations of BEB systems (e.g., a background GOV+K3V binary) can produce blue eclipses while remaining undetected along the line of sight. Such scenarios are constrained by the lack of an observed secondary eclipse and therefore require either eccentric orbits to avoid secondary eclipses or else a background twin-binary system at double the orbital period. The only way to definitively rule out such scenarios is to prove that the loss of light is from the target star, for instance by detecting the Rossiter–McLaughlin (RM) effect during a transit and confirming that the spectroscopic transit is consistent with the photometric transit.

### 3.1.6. Gaia

The “Gaia” curve in Figure 6 combines both point-source detections from imaging and sources showing an astrometric noise excess relative to the single-source astrometric model. The curve was interpolated from Figure 4 of Rizzuto et al. (2018). TOI 837 has a RUWE statistic of 1.022, indicating that there are no obviously present astrometric companions. The unit weight error statistic (square root of the reduced astrometric  $\chi^2$ ) is 1.38, which is consistent with stars of

similar brightness and color (Lindegren et al. 2018, Appendix A).

### 3.1.7. Patient Imaging

Archival SERC-J and AAO-SES plates are available for the TOI 837 field.<sup>31</sup> These plates were acquired in 1982 and 1992, respectively. For high proper motion stars, archival imagery can be used to detect slowly moving background stars that might be an astrophysical false-positive source (e.g., Bakos et al. 2006; Huang et al. 2018a; Vanderburg et al. 2019). However TOI 837 has only moved  $\approx 0''.7$  between 1982 and the present, in comparison to the  $\approx 2''.0$  FWHM of the target on the plates. We therefore cannot resolve it from background sources not already resolved through more modern imaging.

### 3.2. False-positive Probability

The constraints on false-positive scenarios summarized in Figure 6 rule out the possibilities that (i) the eclipses are caused by a star orbiting TOI 837, (ii) the eclipses are caused by hierarchical blends,<sup>32</sup> and (iii) the eclipses are caused by neighboring stars outside  $\approx 2''$ . The only scenario not formally ruled out is a background eclipsing binary. A simple, and fallacious, argument against background blends follows from counting statistics. The local density of  $T < 15.1$  stars around TOI 837, found by counting from TIC8, is  $3.7 \times 10^{-4} \text{ arcsec}^{-2}$ . Therefore within the relevant  $\approx 0''.3$  radius not excluded by the SOAR HRCam contrast curve, for a randomly selected star we would expect  $1.0 \times 10^{-4}$  potential  $T < 15.1$  contaminants, which appears small.

The reason the above statement is an insufficient argument against BEBs is that TOI 837 is not a randomly selected star—it was selected because it shows eclipses. Given a foreground star that shows eclipses, the probability of a background star being present is much greater than that for an arbitrary foreground star. A probabilistic framework is required to calculate the chance that a background eclipsing binary causes the eclipses. We adopt the Bayesian framework implemented in VESPA (Morton 2012, 2015a).

VESPA calculates the FPP for a transit signal as

$$\text{FPP} = 1 - P_{\text{pl}}, \quad (3)$$

where in our case the probability that the signal comes from a planet,  $P_{\text{pl}}$ , is given by

$$P_{\text{pl}} = \frac{\mathcal{L}_{\text{pl}}\pi_{\text{pl}}}{\mathcal{L}_{\text{pl}}\pi_{\text{pl}} + \mathcal{L}_{\text{BEB}}\pi_{\text{BEB}}}, \quad (4)$$

where  $\mathcal{L}_i$  is the model likelihood for the planet and BEB scenarios and  $\pi_i$  is the model prior. The terms labeled as “BEB” usually include other false-positive scenarios (HEBs and EBs), but our follow-up data have excluded these possibilities. The priors are evaluated using a combination of galactic population synthesis (Girardi et al. 2005), binary-star statistics (Raghavan et al. 2010), and specific planet occurrence rates (Morton 2012, Section 3.4). The likelihoods are evaluated by forward-modeling a representative population of eclipsing bodies for each model class, in which each population member has a particular

<sup>31</sup> [https://archive.stsci.edu/cgi-bin/dss\\_form](https://archive.stsci.edu/cgi-bin/dss_form)

<sup>32</sup> There is a small gap in the upper panel of Figure 6 corresponding to a  $\approx 0.7 M_{\odot}$  companion HEB at a projected separation of  $\approx 15$  au. This region of parameter space is small, and we ignore it in the remaining analysis.

<sup>30</sup> <http://svo2.cab.inta-csic.es/theory/fps/>

trapezoidal eclipse depth, total duration, and ingress duration. The likelihood is then calculated by multiplying the probability distribution function of the simulated population’s shape parameters with the posterior probability of the actual observed eclipse shape.

We ran VESPA<sup>33</sup> and directly incorporated our constraints on the SOAR *I*-band contrast curve and a nondetection of secondary eclipses with a depth set at roughly twice the limits from the SPOC vetting report (0.1%). This limit applied across all phases. We verified that changing the secondary-eclipse depth limit did not significantly affect the results. We set the maximum aperture radius at 2", based on our ground-based photometry. Incorporating the constraints from Figure 6, our nominal FPP analysis excluded EB and HEB scenarios. This yielded an FPP of 0.21% for TOI 837b, sufficient for formal validation as a planet (Morton 2012). We did not incorporate our constraint that TOI 837 is not double-lined, which rules out an additional portion of BEB parameter space. Had we not acquired multicolor ground-based photometry and been unable to exclude HEB scenarios, the FPP would have risen to 8%. Since the transits are achromatic (Figure 4), particularly in the Johnson-*B* band, we can rule out HEB scenarios.

One potential caveat in our approach is that VESPA uses a galactic population synthesis to model the sightline. Since TOI 837 is in the foreground of IC 2602 (see Section 4.2), for 25 pc behind the sightline to the star, the number of background stars is higher than VESPA would predict due to the presence of the cluster. To quantify the importance of this effect, we assessed the sky-plane density of potential contaminants by counting stars brighter than  $T = 15.07$  within 0°.5 of TOI 837 (Stassun et al. 2019). We then compared this density against sightlines rotated in galactic longitude toward and away from the galactic center. Within  $\pm 10^\circ$  in galactic longitude, the sky-plane density of stars fluctuated at the level of  $\approx 15\%$ , with a local maximum a few degrees away from TOI 837, toward the center of IC 2602. The overall density also slowly increased toward the galactic center. We therefore do not expect this consideration to significantly alter our FPP calculation.

## 4. System Modeling

### 4.1. The Cluster

#### 4.1.1. Physical Characteristics

The IC 2602 cluster is about 150 pc from the Earth and is near the galactic plane with  $(l, b) \approx (289^\circ.6, -5^\circ.0)$  (Cantat-Gaudin et al. 2018). It is also sometimes called the  $\theta$  Carinae cluster, after its brightest member, or the “Southern Pleiades.” While IC 2602 is close to the Lower Centaurus–Crux subgroup of the Scorpius–Centaurus OB2 association in terms of both position and proper motion space, its older age and clear kinematic separation indicate that it is a distinct stellar population (de Zeeuw et al. 1999; Damiani et al. 2019).

Reliable ages reported for IC 2602 range from 30 to 46 Myr. We have collected ages reported over the years in Table 3. The lithium depletion boundary technique yields slightly older absolute ages than isochrone fitting (Dobbie et al. 2010; Randich et al. 2018). Rather than redetermine the age of the cluster and add another line to the table, we simply adopt an absolute-age range for TOI 837 of 30–46 Myr.

**Table 3**  
Previously Reported Ages for the Open Cluster IC 2602

Method	Age (Myr)	Reference
MSTO isochrone	36.3	Mermilliod (1981)
PMS+MSTO isochrone	30 $\pm$ 5	Stauffer et al. (1997)
Isochrone (a)	67.6	Kharchenko et al. (2005)
Isochrone (b)	221	Kharchenko et al. (2013)
Isochrone	67.6	van Leeuwen (2009)
LDB (c)	46 $^{+5}_{-7}$	Dobbie et al. (2010)
MSTO isochrone (d)	41–46	David & Hillenbrand (2015)
MSTO isochrone (e)	37–43	David & Hillenbrand (2015)
Li selection + isochrone	43.7 $^{+4.3}_{-3.9}$	Bravi et al. (2018)
Isochrone (f)	30 $^{+9}_{-7}$	Randich et al. (2018)
LDB	43.7 $^{+4.3}_{-3.9}$	Randich et al. (2018)
Isochrone	35.5 $^{+0.8}_{-1.6}$	Bossini et al. (2019)
Isochrone	35.5 $^{+14.6}_{-10.4}$	Kounkel & Covey (2019)

**Note.** MSTO  $\equiv$  main-sequence turn-off. PMS  $\equiv$  pre-main-sequence. LDB  $\equiv$  lithium depletion boundary. (a) Based on location in Hertzsprung–Russell (HR) diagram of just two stars. (b) Notes major age change since Kharchenko et al. (2005). (c) Dobbie et al. (2010) performed a dedicated study of the LDB in IC 2602. Their resulting LDB age was slightly larger than previously reported isochrone ages, which they noted is consistent with similar discrepancies seen in the Pleiades,  $\alpha$ -Per, IC 2391, and NGC 2457. (d) Using Ekström et al. (2012) evolutionary models. (e) Using PARSEC evolutionary models (Bressan et al. 2012). (f) Averaged across PROSECCO, PARSEC, and MIST models in  $(J, H, K_s)$  and  $(J, H, K_s, V)$  planes.

Reported mean metallicity values [Fe/H] for the cluster range between slightly supersolar ( $0.04 \pm 0.01$ ; Baratella et al. 2020) and slightly subsolar ( $-0.02 \pm 0.02$ ; Netopil et al. 2016). The extinction  $E(B - V)$  is rather low, with reported values ranging from 0.03 to 0.07 (e.g., Randich et al. 2018).

Kinematically, IC 2602 seems to be supervirial, in the sense that the observed stellar velocity dispersion is larger than the value expected if it were in virial equilibrium by about a factor of two (Bravi et al. 2018). Damiani et al. (2019) also reported evidence for the ongoing evaporation of IC 2602, in the form of a diffuse  $\approx 10^\circ$  halo of young stars around the central density cusps. A gyrochronological study of these stars could confirm that these stars are truly coeval with the cluster.

#### 4.1.2. HR Diagram

Figure 7 shows an HR diagram of TOI 837, the IC 2602 cluster, and the neighborhood of spatially nearby stars. Stars labeled as cluster members are those reported by Cantat-Gaudin et al. (2018) based on Gaia DR2 positions, proper motions, and parallaxes. We included candidate members with a formal membership probability exceeding 10%. Most members appear to be young and coeval. TOI 837 lies on the single-star sequence. Any hypothetical companions to TOI 837 must therefore have  $\lesssim 50\%$  of its brightness; brighter companions would have made the total system  $\gtrsim 0.44$  mag brighter than the single-star sequence, which can be ruled out based on the photometric uncertainties and the intrinsic scatter in the HR diagram.

Figure 7 suggests that the membership census of IC 2602 is incomplete. We defined the reference neighborhood as the group of at most  $10^4$  randomly selected non-member stars within five standard deviations of the mean IC 2602 R.A., decl., and parallax. In other words, the neighborhood members

<sup>33</sup> We used VESPA-0.6 and isochrones-1.2.2.

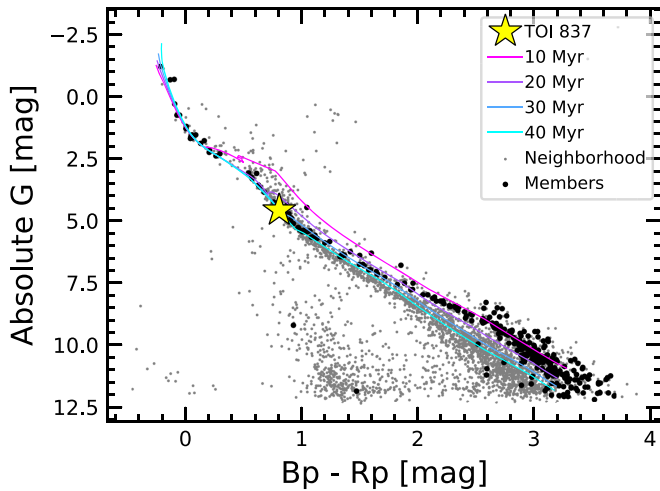


**Figure 7.** HR diagram of TOI 837 and members of IC 2602. The members (black circles) were identified by Cantat-Gaudin et al. (2018). The gray circles are non-member stars with R.A., decl., and parallax similar to those of IC 2602. They were selected by drawing from an  $\{\alpha, \delta, \pi\}$  cube centered on the cluster with boundaries set at  $5\times$  the standard deviation in the cluster parameters.  $G$  denotes Gaia broadband magnitudes,  $Bp$  Gaia blue, and  $Rp$  Gaia red. MIST isochrones (colored lines) fit the upper main sequence well but diverge from the data for  $M_* \lesssim 0.7 M_\odot$ . This is a known issue with M-dwarf models (see Section 4.1.2).

were chosen based on the observed spread in the cluster’s parameters. We queried Gaia DR2 for these stars using *astroquery* (Ginsburg et al. 2018). Many low-mass stars appeared above the main sequence, even though they were not identified as five-dimensional kinematic members through the unsupervised Cantat-Gaudin et al. (2018) membership assignment process.

Figure 7 also compares the data to the MIST isochrones (Choi et al. 2016). We used the web interface<sup>34</sup> to interpolate isochrones at 10, 20, 30, and 40 million years. We assumed solar metallicity and a fixed extinction value of  $A_V = 0.217$  (Randich et al. 2018). The 30 and 40 Myr models align well with the data for stars with masses of roughly  $0.7\text{--}7 M_\odot$ . The PMS K- and M-dwarf models are bluer than observed in the Gaia photometry. This discrepancy was noted and discussed at length by Choi et al. (2016). One suggested explanation was that strong magnetic fields in low-mass PMS stars inhibit convection and produce a high filling factor of starspots (e.g., Stauffer et al. 2003; Feiden & Chaboyer 2013). This explanation however fails to explain poor isochrone fits in both old open clusters (e.g., M67) and the field, particularly in blue bandpasses. An alternative explanation is that the molecular line lists for M-dwarf atmospheres are incomplete in these wavelength ranges (Mann et al. 2013; Rajpurohit et al. 2013).

## 4.2. The Star

### 4.2.1. Membership of TOI 837 in IC 2602

TOI 837 has been reported as a member of IC 2602 by many independent investigators (e.g., Kharchenko et al. 2013; Oh et al. 2017; Cantat-Gaudin et al. 2018; Damiani et al. 2019; Kounkel & Covey 2019). The simplest way to verify the membership is through inspection of the Gaia DR2 position

and kinematics. Figure 8 shows the six-dimensional positions and kinematics of TOI 837, IC 2602 members, and nearby stars. The “neighborhood” is defined as in Figure 7. The axis limits for the R.A., decl., and parallax dimensions are set to within five standard deviations of the mean IC 2602 R.A., decl., and parallax. The axis limits for the proper motion and RV dimensions are set at the 25th and 75th percentiles, in order to give a sense of the population’s distribution while excluding outliers. The RVs suffer the greatest incompleteness due to the current  $G \approx 12$  mag limit of the Gaia DR2 data processing.

Figure 8 provides strong evidence that TOI 837 is a member of IC 2602. The only dimension that could lead to some doubt is the parallax, as TOI 837 is one of the closest IC 2602 members reported by Cantat-Gaudin et al. (2018). Fortunately, there are independent means of verifying the star’s youth.

### 4.2.2. Rotation

As stars get older, their rotation rates incrementally slow due to magnetic braking (Skumanich 1972; Weber & Davis 1967). One way to verify the youth of TOI 837 is by comparing its rotation period to those of other stars with known ages.

We measured the rotation period from the TESS PDCSAP light curve using the Lomb–Scargle periodogram implemented in *astropy* (Lomb 1976; Scargle 1982; VanderPlas & Ivezić 2015). We fitted the light curve without masking out the transits or flares, as these represented a small fraction of the overall time series. To derive the uncertainty on the best period, we fitted a Gaussian to the dominant peak, after first ensuring that we had oversampled the initial frequency grid. This gave a rotation period of  $P_{\text{rot}} = 2.987 \pm 0.056$  days when allowing for a single Fourier term in the periodogram model, and  $P_{\text{rot}} = 3.004 \pm 0.053$  days when allowing for two Fourier terms. As the latter model provides a better fit to the data, we adopt it as the rotation period.

As we discuss in Section 4.2.4, we measured the star’s radius by combining the spectroscopic effective temperature with a broadband photometry spectral energy distribution (SED) fit. We would expect, by combining our  $R_*$  and  $P_{\text{rot}}$  measurements, that the equatorial velocity  $v$  of the star would be  $17.67 \pm 0.32 \text{ km s}^{-1}$ . Our spectroscopically measured  $v \sin i$  from CHIRON,  $16.2 \pm 1.1 \text{ km s}^{-1}$ , agrees reasonably well with this expectation.

The star is clearly a rapid rotator. Figure 9 compares its rotation period with rotation periods that have been measured in a number of well-studied open clusters. TOI 837 seems to be gyrochronologically coeval with the Pleiades sequence. This is not to say that TOI 837 is “Pleiades-aged,” because the observed scatter in the rotation period diagram for the first 10–100 Myr is quite high (see Figure 9 of Rebull et al. 2020). Instead, we interpret the rotation period as evidence to support the claim that TOI 837 is younger than  $\sim 500$  Myr.

### 4.2.3. Lithium

Lithium depletion for early G dwarfs like TOI 837 requires hundreds of megayears (Soderblom et al. 2014). This is because their convective envelopes are shallow, and so transport of photospheric lithium to the hot core takes place over diffusive timescales, rather than convective timescales. Nonetheless, comparison of early G dwarfs in the field to, e.g., 600 Myr old Hyads has shown that the depletion does indeed happen over many gigayears (Berger et al. 2018).

<sup>34</sup> [http://waps.cfa.harvard.edu/MIST/interp\\_isos.html](http://waps.cfa.harvard.edu/MIST/interp_isos.html), 2020-07-08.

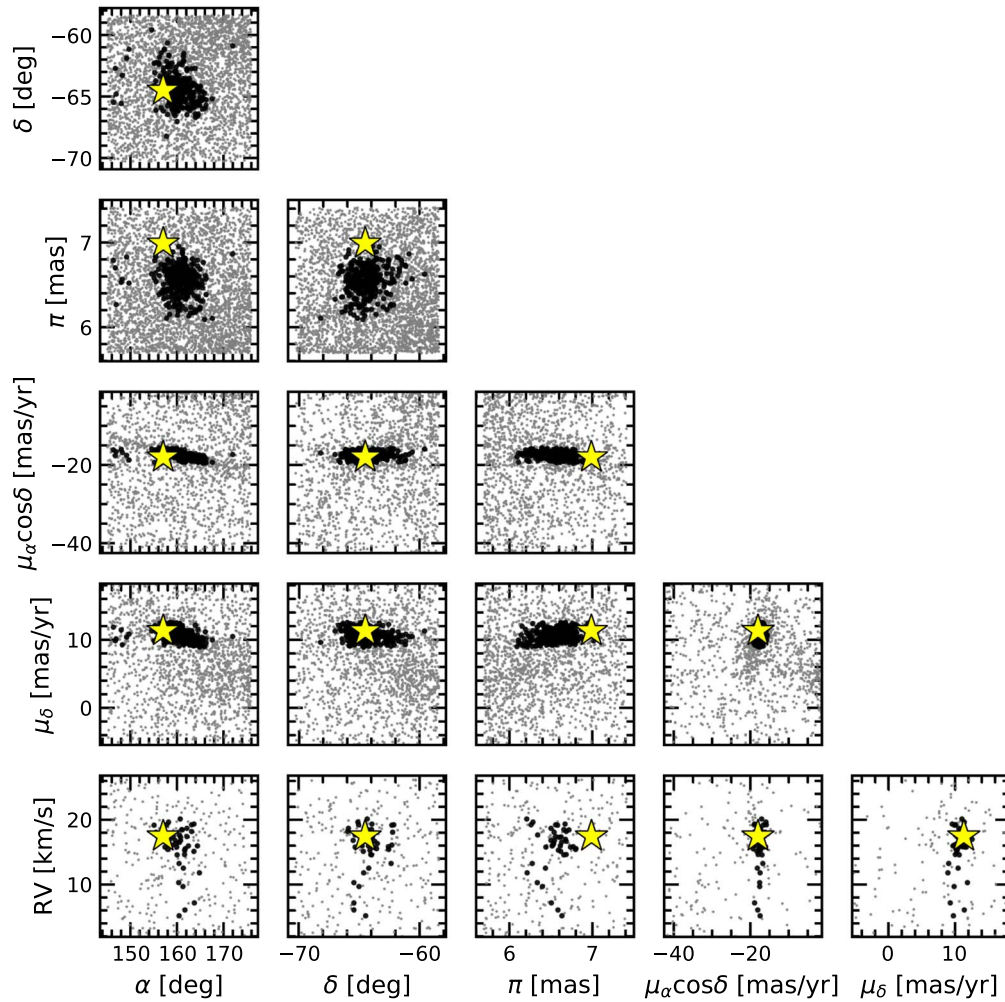


**Figure 8.** Positions and kinematics of TOI 837 (star), IC 2602 members (black circles), and stars in the neighborhood (gray circles). Members were identified by Cantat-Gaudin et al. (2018). Neighbors are as in Figure 7. The symbol  $\alpha$  denotes R.A.,  $\delta$  decl.,  $\pi$  parallax, and  $\mu_\delta$  and  $\mu_\alpha$  the proper motion in each equatorial direction; RV denotes the RVs reported by Gaia DR2. The RVs are for unblended spectra of bright stars ( $G \lesssim 12$ ). The proper-motion projection ( $\mu_\delta$  vs.  $\mu_\alpha \cos \delta$ ) highlights the incompleteness in the membership selection function.

The spectra of TOI 837 all show the 6708 Å lithium doublet in absorption. Opting to use our FEROS spectra because of their high S/N, we measured the line’s EW to be  $154 \pm 9$  mÅ. Figure 9 compares this EW to those of stars in the field and other young open cluster members. The field star measurements were collected by Berger et al. (2018); we show their reported lithium detections with  $S/N > 3$ . The young open cluster members were selected based on the presence of lithium, as described by Randich et al. (2018). The measured TOI 837 lithium EW is much larger than those observed for field stars and is consistent with the lithium absorption seen in stars with similar colors in sub-100 Myr moving groups.

#### 4.2.4. Stellar Parameters

Select properties of TOI 837 from the literature and our analysis are presented in Table 4. We calculated the stellar parameters using two different approaches.

In “Method 1,” we measured the spectroscopic parameters from each of the CHIRON spectra (Section 2.5.1). We then calculated the stellar radius and reddening following Stassun et al. (2017). We first derived the bolometric flux by combining available broadband

magnitudes from Gaia, Tycho-2, the AAVSO Photometric All-sky Survey, the Two Micron All Sky Survey (2MASS), and the Wide-field Infrared Survey Explorer (WISE). We then fitted the SED with the Kurucz (2013) stellar atmosphere models and summed it to find  $F_{\text{bol}}$ . When fitting the atmosphere model, we varied the extinction ( $A_V$ ) and the overall normalization. This procedure yielded  $A_V = 0.20 \pm 0.03$ , which agrees with the average from the IC 2602 isochrone fits of Randich et al. (2018). Combining the spectroscopic effective temperature, bolometric flux, and Gaia distance, we determined the stellar radius using the Stefan–Boltzmann law. Combining this radius with the spectroscopic  $\log g$  also yielded a stellar mass. The stellar mass however seemed to be high relative to the observed CHIRON effective temperature ( $1.21 M_\odot$  to 5946 K, with relative uncertainties of a few percent on each). We therefore explored a second method and ultimately adopted it because its systematic uncertainties were easier to quantify.

In “Method 2,” we used the observed location of TOI 837 in the HR diagram and interpolated it against the 40 Myr MIST isochrone. This method leverages the relative location of TOI 837 within the IC 2602 isochrone to derive precise,

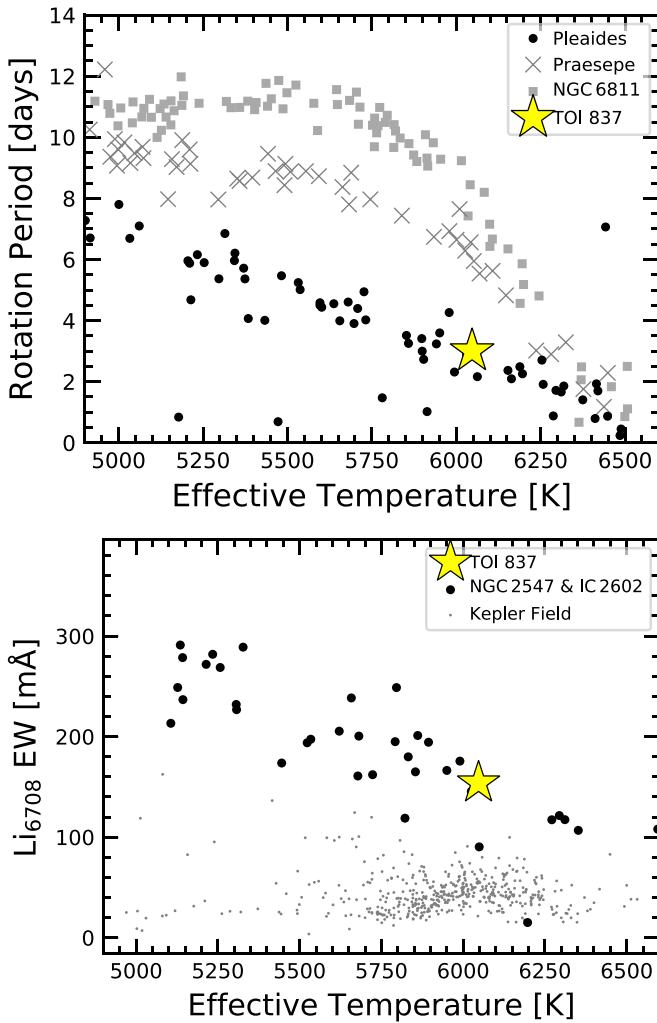


**Figure 9.** Youth diagnostics. Top: Rotation periods for TOI 837 and selected open clusters. The Pleiades (120 Myr), Praesepe (670 Myr), and NGC 6811 (1000 Myr) are shown. Their rotation periods were measured by Rebull et al. (2016), Douglas et al. (2017, 2019), and Curtis et al. (2019a), respectively. Bottom: Lithium 6708 Å equivalent widths (EWs) for TOI 837, field stars, and young open clusters. The field star sample was drawn from Kepler planet hosts and was measured by Berger et al. (2018) using Keck’s High Resolution Echelle Spectrometer. The young open cluster members were surveyed by Randich et al. (2018) using the Ultraviolet and Visual Echelle Spectrograph and the GIRAFFE spectrograph at the ESO’s Very Large Telescope. Randich et al. (2018) found lithium depletion boundary ages for these clusters of  $37.7^{+3.7}_{-4.8}$  Myr (NGC 2547) and  $43.7^{+4.3}_{-3.9}$  Myr (IC 2602).

theoretically self-consistent constraints on all of the stellar parameters. Although this approach would fail for a low-mass star, TOI 837 is above the stellar masses where the Gaia photometry and isochrone models begin to diverge. The statistical uncertainties yielded by this approach are of order 1% for the stellar mass and radius. To quantify the systematic uncertainties, we compared the parameters derived from the MIST isochrones with those from the PARSEC<sup>35</sup> isochrones (Bressan et al. 2012; Chen et al. 2014, 2015; Marigo et al. 2017). The PARSEC isochrones gave a stellar mass 5% lower, an effective temperature 3% lower, a logarithmic surface gravity 1% lower, and a radius 8% smaller than that given by the MIST isochrones. For the sake of self-consistency, in Table 4 and in the ensuing analysis we adopt the stellar

**Table 4**  
Literature and Measured Properties for TOI 837

Other Identifiers			
	TIC 460205581		
	GAIADR2 5251470948229949568		
Parameter	Description	Value	Source
$\alpha_{J2015.5}$	R.A. (hh:mm:ss)	10:28:08.95	1
$\delta_{J2015.5}$	Decl. (dd:mm:ss)	−64:30:18.76	1
$l_{J2015.5}$	Galactic longitude (deg)	288.2644	1
$b_{J2015.5}$	Galactic latitude (deg)	−5.7950	1
$B$	Johnson- $B$ mag.	$11.119 \pm 0.107$	2
$V$	Johnson- $V$ mag.	$10.635 \pm 0.020$	2
$G$	Gaia- $G$ mag.	$10.356 \pm 0.020$	1
$Bp$	Gaia- $Bp$ mag.	$10.695 \pm 0.020$	1
$Rp$	Gaia- $Rp$ mag.	$9.887 \pm 0.020$	1
$T$	TESS mag.	$9.9322 \pm 0.006$	2
$J$	2MASS- $J$ mag.	$9.392 \pm 0.030$	3
$H$	2MASS- $H$ mag.	$9.108 \pm 0.038$	3
$K_s$	2MASS- $K_s$ mag.	$8.933 \pm 0.026$	3
W1	WISE1 mag.	$8.901 \pm 0.023$	4
W2	WISE2 mag.	$8.875 \pm 0.021$	4
W3	WISE3 mag.	$8.875 \pm 0.020$	4
W4	WISE4 mag.	$8.936 \pm \text{N/A}$	4
$\pi$	Gaia DR2 parallax (mas)	$6.989 \pm 0.022$	1
$d$	Distance (pc)	$143.1 \pm 0.5$	1
$\mu_\alpha$	Gaia DR2 proper motion in R.A. (mas yr <sup>−1</sup> )	$−18.017 \pm 0.039$	1
$\mu_\delta$	Gaia DR2 proper motion in decl. (mas yr <sup>−1</sup> )	$11.307 \pm 0.037$	1
RV	Systemic RV (km s <sup>−1</sup> )	$17.44 \pm 0.64^a$	1
$v \sin i_*$	RV (km s <sup>−1</sup> )	$16.2 \pm 1.1$	5
$v_{\text{mac}}$	Macroturbulence velocity (km s <sup>−1</sup> )	$8.4 \pm 2.9$	5
[Fe/H]	Metallicity	$−0.069 \pm 0.042$	5
$T_{\text{eff}}$	Effective temperature (K)	$6047 \pm 162$	6
$\log g_*$	Surface gravity (cgs)	$4.467 \pm 0.049$	6
Li EW	6708 Å EW (mÅ)	$154 \pm 9$	7
$P_{\text{rot}}$	Rotation period (day)	$3.004 \pm 0.053$	8
Age	Adopted stellar age (Myr)	30–46	9
Spec. type	Spectral type	G0/F9 V	5
$R_*$	Stellar radius ( $R_\odot$ )	$1.022 \pm 0.083$	6
$M_*$	Stellar mass ( $R_\odot$ )	$1.118 \pm 0.059$	6
$A_v$	Interstellar reddening (mag)	$0.20 \pm 0.03$	10

#### Notes.

<sup>a</sup> Systemic RV uncertainty is the standard deviation of single-transit RVs, as quoted from Gaia DR2. The sources are (1) Gaia Collaboration et al. (2018), (2) Stassun et al. (2019), (3) Skrutskie et al. (2006), (4) Wright et al. (2010), (5) CHIRON spectra, (6) Method 2 (cluster isochrone, Section 4.2.4), (7) FEROS spectra, (8) TESS light curve, (9) IC 2602 ages from isochrone and lithium depletion analyses (Section 4.1.1), and (10) Method 1 (photometric SED fit, Section 4.2.4).

parameter values from MIST. We took the uncertainties to be the quadrature sum of the statistical and systematic components.

#### 4.3. The Planet

We also considered two different approaches for fitting the available time-series photometry of TOI 837b. In the first

<sup>35</sup> <http://stev.oapd.inaf.it/cmd>

**Table 5**  
Priors and Posteriors for the Model Fitted to the TESS and Ground-based Data

Param.	Unit	Prior	Median	Mean	Std. Dev.	3%	97%
<i>Sampled: physical</i>							
$P$	day	$\mathcal{N}(8.3249; 0.1000)$	8.3248762	8.3248762	0.0000157	8.3248466	8.3249057
$t_0^a$	day	$\mathcal{N}(1574.273800; 0.1000)$	1574.272527	1574.2725263	0.0005931	1574.2713991	1574.273626
$\log R_p/R_*$	...	$\mathcal{U}(-4.605; 0.000)$	-2.58156	-2.56901	0.06659	-2.67426	-2.44791
$b$	...	$\mathcal{U}(0; 1 + R_p/R_*)$	0.9358	0.9374	0.0127	0.9164	0.9615
$u_1$	...	$\mathcal{U}(0.175; 0.475)^b$	0.344	0.338	0.085	0.199	0.475
$u_2$	...	$\mathcal{U}(0.085; 0.385)^b$	0.251	0.245	0.085	0.108	0.385
$R_*$	$R_\odot$	$\mathcal{T}(1.022; 0.083)$	1.042	1.042	0.076	0.902	1.189
$\log g$	cgs	$\mathcal{N}(4.467; 0.049)$	4.451	4.451	0.042	4.372	4.528
<i>Sampled: nuisance</i>							
$a_{00}$ :TESS	...	$\mathcal{N}(1.00; 0.01)$	0.9986	0.9986	0.0001	0.9984	0.9987
$a_{01}$ :TESS	day <sup>-1</sup>	$\mathcal{U}(-0.05; 0.05)$	-0.0004	-0.0004	0.0003	-0.0010	0.0003
$a_{02}$ :TESS	day <sup>-2</sup>	$\mathcal{U}(-0.05; 0.05)$	-0.0183	-0.0183	0.0023	-0.0226	-0.0141
$a_{10}$ :TESS	...	$\mathcal{N}(1.00; 0.01)$	1.0090	1.0090	0.0001	1.0088	1.0092
$a_{11}$ :TESS	day <sup>-1</sup>	$\mathcal{U}(-0.05; 0.05)$	-0.0138	-0.0138	0.0003	-0.0144	-0.0132
$a_{12}$ :TESS	day <sup>-2</sup>	$\mathcal{U}(-0.05; 0.05)$	-0.0550	-0.0550	0.0022	-0.0591	-0.0508
$a_{20}$ :TESS	...	$\mathcal{N}(1.00; 0.01)$	0.9992	0.9992	0.0001	0.9990	0.9993
$a_{21}$ :TESS	day <sup>-1</sup>	$\mathcal{U}(-0.05; 0.05)$	0.0156	0.0156	0.0004	0.0150	0.0163
$a_{22}$ :TESS	day <sup>-2</sup>	$\mathcal{U}(-0.05; 0.05)$	0.0232	0.0232	0.0024	0.0187	0.0276
$a_{30}$ :TESS	...	$\mathcal{N}(1.00; 0.01)$	1.0013	1.0013	0.0001	1.0011	1.0015
$a_{31}$ :TESS	day <sup>-1</sup>	$\mathcal{U}(-0.05; 0.05)$	0.0021	0.0021	0.0004	0.0014	0.0028
$a_{32}$ :TESS	day <sup>-2</sup>	$\mathcal{U}(-0.05; 0.05)$	-0.0097	-0.0097	0.0029	-0.0150	-0.0043
$a_{40}$ :TESS	...	$\mathcal{N}(1.00; 0.01)$	0.9906	0.9906	0.0001	0.9905	0.9908
$a_{41}$ :TESS	day <sup>-1</sup>	$\mathcal{U}(-0.05; 0.05)$	0.0015	0.0015	0.0003	0.0009	0.0022
$a_{42}$ :TESS	day <sup>-2</sup>	$\mathcal{U}(-0.05; 0.05)$	0.0313	0.0313	0.0023	0.0269	0.0356
$a_{00}$ :Sauce	...	$\mathcal{N}(1.00; 0.01)$	0.9996	0.9996	0.0001	0.9993	0.9998
$a_{01}$ :Sauce	day <sup>-1</sup>	$\mathcal{U}(-0.05; 0.05)$	-0.0041	-0.0041	0.0023	-0.0085	0.0002
$a_{02}$ :Sauce	day <sup>-2</sup>	$\mathcal{U}(-0.05; 0.05)$	0.0311	0.0256	0.0205	-0.0135	0.0500
$a_{10}$ :Sauce	...	$\mathcal{N}(1.00; 0.01)$	0.9998	0.9998	0.0001	0.9996	1.0000
$a_{11}$ :Sauce	day <sup>-1</sup>	$\mathcal{U}(-0.05; 0.05)$	-0.0004	-0.0004	0.0021	-0.0044	0.0035
$a_{12}$ :Sauce	day <sup>-2</sup>	$\mathcal{U}(-0.05; 0.05)$	0.0360	0.0314	0.0165	0.0005	0.05000
$a_{20}$ :Sauce	...	$\mathcal{N}(1.00; 0.01)$	0.9999	0.9999	0.0001	0.9996	1.0001
$a_{21}$ :Sauce	day <sup>-1</sup>	$\mathcal{U}(-0.05; 0.05)$	-0.0009	-0.0009	0.0030	-0.0066	0.0046
$a_{22}$ :Sauce	day <sup>-2</sup>	$\mathcal{U}(-0.05; 0.05)$	0.0067	0.0047	0.0278	-0.0410	0.0500
$a_{30}$ :Sauce	...	$\mathcal{N}(1.00; 0.01)$	0.9996	0.9996	0.0003	0.9991	1.0001
$a_{31}$ :Sauce	day <sup>-1</sup>	$\mathcal{U}(-0.05; 0.05)$	0.0047	0.0047	0.0069	-0.0084	0.0176
$a_{32}$ :Sauce	day <sup>-2</sup>	$\mathcal{U}(-0.05; 0.05)$	0.0077	0.0052	0.0286	-0.0419	0.0500
$a_{00}$ :ASTEP	...	$\mathcal{N}(1.00; 0.01)$	0.9996	0.9996	0.0001	0.9994	0.9998
$a_{01}$ :ASTEP	day <sup>-1</sup>	$\mathcal{U}(-0.05; 0.05)$	0.0022	0.0022	0.0007	0.0010	0.0035
$a_{02}$ :ASTEP	day <sup>-2</sup>	$\mathcal{U}(-0.05; 0.05)$	0.0073	0.0074	0.0076	-0.0067	0.0219
$a_{10}$ :ASTEP	...	$\mathcal{N}(1.00; 0.01)$	1.0000	1.0000	0.0001	0.9998	1.0002
$a_{11}$ :ASTEP	day <sup>-1</sup>	$\mathcal{U}(-0.05; 0.05)$	0.0042	0.0042	0.0010	0.0024	0.0061
$a_{12}$ :ASTEP	day <sup>-2</sup>	$\mathcal{U}(-0.05; 0.05)$	0.0164	0.0162	0.0145	-0.0105	0.0439
$a_{20}$ :ASTEP	...	$\mathcal{N}(1.00; 0.01)$	0.9993	0.9993	0.0001	0.9991	0.9995
$a_{21}$ :ASTEP	day <sup>-1</sup>	$\mathcal{U}(-0.05; 0.05)$	-0.0074	-0.0074	0.0016	-0.0103	-0.0044
$a_{22}$ :ASTEP	day <sup>-2</sup>	$\mathcal{U}(-0.05; 0.05)$	0.0204	0.0173	0.0216	-0.0209	0.0500
<i>Derived</i>							
$R_p/R_*$	...	...	0.08	0.08	0.01	0.07	0.09
$\rho_*$	g cm <sup>-3</sup>	...	1.40	1.40	0.15	1.13	1.68
$R_p$	$R_{\text{Jup}}$	...	0.77	0.78	0.09	0.62	0.95
$a/R_*$	...	...	17.26	17.24	0.60	16.12	18.36
$\cos i$	...	...	0.054	0.054	0.003	0.050	0.059
$T_{14}$	hr	...	1.957	1.955	0.039	1.887	2.032
$T_{13}$	hr	...	0.30	0.30	0.13	0.004	NaN <sup>c</sup>

**Notes.**

<sup>a</sup> The most precise ephemeris based on the combination of TESS and ground-based data is also shown in Equation (11).

<sup>b</sup> Assuming an informative quadratic limb-darkening prior with values about those given for the appropriate  $T_{\text{eff}}$  and  $\log g$  in the TESS band from Claret (2017). The precision achieved in the ground-based data did not appear to necessitate using bandpass-dependent limb-darkening coefficients.

<sup>c</sup> The second and third contact points do not exist for a grazing transit. Notation:  $a_{ij:\text{instr}}$  denotes the  $i$ th transit of a particular instrument and the  $j$ th polynomial detrending order.  $\mathcal{U}$  denotes a uniform distribution,  $\mathcal{N}$  a normal distribution, and  $\mathcal{T}$  a truncated normal bounded between zero and an upper limit much larger than the mean.

approach, we fitted the ground- and space-based transits simultaneously. In the second, we fitted the TESS data alone.

To clean the TESS PDCSAP light curve, we first eliminated points that had quality flags corresponding to any of bits {3, 4, 6, 8, 11, 12}. This excluded cadences affected by coarse spacecraft pointing, reaction wheel desaturation events, manual flags, cosmic-ray hits, and stray light from the Earth or Moon being present. Inspecting the data, we also manually excluded the two flares shown in Figure 1. We then trimmed the TESS data to windows of  $\pm 7$  hr centered on each transit.

Our model for the time-series photometry data was an Agol et al. (2020) transit with physical and orbital parameters shared across all transit windows, plus a local quadratic trend allowed within each window. Select parameters and priors are listed in Table 5 for the joint model of the TESS and ground-based data. In brief, we fitted for the shared stellar parameters  $\{\log g, R_*, u_0, u_1\}$  and the shared planetary parameters  $\{t_0, P, b, \log(R_p/R_*)\}$ . There were also three free trend parameters for each transit window to account for the local rotational variability. In the TESS-only model this yielded 23 free parameters, of which 8 were physically relevant and 15 were nuisance parameters. In the combined TESS and ground-based model, there were an additional seven transits and therefore an additional 21 nuisance parameters for a total of 44 free parameters.

We fitted the models using PyMC3 (Salvatier et al. 2016; Theano Development Team 2016). For the exoplanet transit, we used the `exoplanet` code (Foreman-Mackey et al. 2020). After initializing each model with the parameters of the maximum a posteriori model, we assumed a Gaussian likelihood and sampled using PyMC3’s gradient-based No-U-Turn Sampler (Hoffman & Gelman 2014). We used  $\hat{R}$  as our convergence diagnostic (Gelman & Rubin 1992).

We opted for this approach rather than a joint fit of the photometry and RVs because the RVs on their own did not show evidence for a planetary signal. Our assumption of a constant radius across all bandpasses was tested by independently fitting each ground-based transit while letting the planetary radius float (Section 3.1.5). The transit depths did not significantly change between different bandpasses. Our assumption in the FPP calculation (Section 3.2) of no odd–even variations was tested by independently fitting all odd and all even transits separately. The resulting best-fit depths were consistent within  $1\sigma$ .

The posteriors from fitting the TESS and ground-based data are given in Table 5. The condition for a grazing transit is whether the impact parameter  $b$  is above  $1 - R_p/R_*$ . The relevant posterior probabilities are shown in Figure 10. The transit is either grazing or nearly grazing. The planet radius and impact parameter based on the TESS and ground-based data are as follows:

$$R_p = 0.768_{-0.072}^{+0.091} R_{\text{Jup}}, \quad (5)$$

$$b = 0.936_{-0.010}^{+0.013}, \quad (6)$$

where we quote the median, 86th, and 14th percentiles of the marginalized one-dimensional posteriors. The second model, which used just the TESS data and the cluster-isochrone stellar parameter priors, formally yielded only a one-sided limit on the planet radius. The reason is that the  $b$ – $R_p/R_*$  degeneracy was not broken: the combination of uncertain stellar parameters and

the grazing geometry allowed very high planet-to-star radius ratios for very large impact parameters. Based on our mass upper limit of  $1.20 M_{\text{Jup}}$ , we might argue in favor of discarding the large-radius solution, since no sub-Jovian mass objects larger than  $\sim 3R_{\text{Jup}}$  are known to exist. Had we imposed this additional prior, then the TESS-only model would have yielded

$$R_p = 0.836_{-0.121}^{+0.208} R_{\text{Jup}} \quad (7)$$

$$b = 0.957_{-0.017}^{+0.027}. \quad (8)$$

Although these parameters are in  $1\sigma$  agreement with our adopted joint model of the TESS and ground-based data, we preferred the first model both because it included all available data and because it succeeded in breaking the  $b$ – $R_p/R_*$  degeneracy without requiring the adoption of informed priors.

## 5. Discussion

TOI 837 joins a number of other young planetary systems reported from TESS, including DS Tuc Ab, HIP 67522b, TOI 1726, and AU Mic b (Newton et al. 2019; Addison et al. 2020; Hirano et al. 2020; Mann et al. 2020; Martioli et al. 2020; Montet et al. 2020; Palle et al. 2020; Plavchan et al. 2020; Rizzuto et al. 2020; Zhou et al. 2020). In the space of planet sizes and ages, the top panel of Figure 11 shows that TOI 837 is among the youngest transiting planets known. In the space of planet sizes and orbital periods, the bottom panel of Figure 11 highlights a peculiar feature of known sub-100 Myr transiting planets: they do not overlap with the known populations of either hot Jupiters or sub-Neptune-sized planets. The young planets instead have sizes ranging from  $4.2 R_{\oplus}$  (AU Mic b) to slightly smaller than Jupiter. The lack of sub-Neptune-sized planets could be a selection effect, because larger planets are easier to detect around highly variable stars. Another (speculative) explanation is that known sub-100 Myr planets are currently enveloped by primordial H/He atmospheres and that they will become sub-Neptune-sized planets after undergoing atmospheric escape (e.g., Fortney et al. 2007; Owen & Wu 2013; Gupta & Schlichting 2019, 2020).

While we have statistically validated that TOI 837 is a planet, the possibility that it could be a background eclipsing binary has not been excluded with sufficient confidence to call the planet “confirmed.” The distinction is methodological. Our calculations have shown that at the population level we expect negligibly few BEBs within  $\approx 0.3$  of TOI 837 to produce eclipses of the appropriate shape across all bandpasses, with no observed secondary eclipse or odd–even variations. This statement is tautologically “validation,” but it is weaker than having data on hand that conclusively rules in favor of the planetary interpretation.

The easiest way to confirm the planetary nature of TOI 837 will be an RM measurement. Detection of an RM signal consistent with the photometric transit would rule out BEB and HEB scenarios, as it would imply that the eclipsing object is bound to the target star. Combined with our nondetection of the planet’s mass from RV monitoring, this would confirm that TOI 837b is a planet.

The maximum amplitude of the RM anomaly is (Gaudi & Winn 2007)

$$\Delta V_{\text{RM}} \approx f_{\text{LD}} \cdot \delta \cdot v \sin i \cdot \sqrt{1 - b^2} \approx 14 \text{ m s}^{-1}, \quad (9)$$

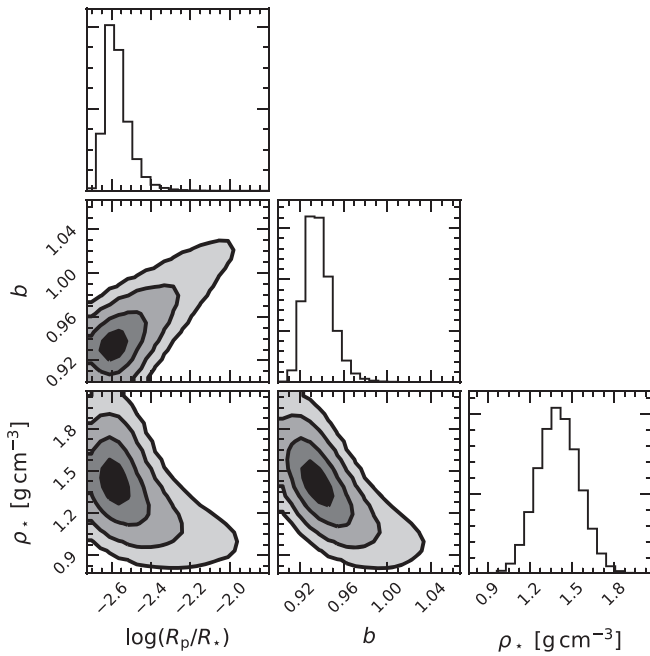


**Figure 10.** Posterior probabilities of impact parameter, planet-to-star size ratio, and stellar density. Contours are shown at  $1\sigma$ ,  $2\sigma$ ,  $3\sigma$ , and  $4\sigma$  confidence. The planet-to-star size ratio corresponds to a planet size between  $0.62 R_{\text{Jup}}$  and  $0.95 R_{\text{Jup}}$  (3rd–97th percentile). This plot was made using `corner` (Foreman-Mackey 2016).

for

$$f_{\text{LD}} = 1 - u_1(1 - \mu) - u_2(1 - \mu)^2, \quad (10)$$

where  $\mu \approx (1 - b^2)^{1/2}$ ,  $u_i$  denotes the limb-darkening parameter, and for calculation purposes we assumed  $b = 0.95$  and used the stellar and transit parameters from Tables 4 and 5. Although challenging, for a 1.9 hr transit of a  $V = 10.6$  star, a detection could be achieved with modern spectrographs. The next viable total transit windows from Chile will occur in 2021 January and February; there are also a few visible per season from other southern locations. The most precise available ephemeris, found from our joint fit of the TESS and ground-based photometry, is as follows:

$$\begin{aligned} t_0 [\text{BJD}_{\text{TDB}}] &= 2458574.272527 \pm 0.000593 \\ P [\text{day}] &= 8.3248762 \pm 0.0000157 \\ T_{14} [\text{hr}] &= 1.96 \pm 0.04. \end{aligned} \quad (11)$$

The RM approach is more likely to yield short-term success than a direct mass measurement because of the RV noise expected to be induced by stellar rotation. The photometric amplitude induced by starspots on TOI 837 is  $\approx 2\%$ . The spot-induced RV variation expected over the course of the  $\approx 3$  day rotation period can be estimated by multiplying the photometric amplitude and spectroscopic equatorial velocity. This gives  $\sigma_{\text{RV,rot}} \approx 300 \text{ m s}^{-1}$  and is consistent with the scatter we observed in our RVs from FEROS. Detecting a planet’s Keplerian motion in this regime is challenging and requires a significant amount of data and care in signal extraction (Barragán et al. 2019; Stefansson et al. 2020). RM measurement avoids the majority of this issue because the transit occurs over a much shorter duration than a single stellar rotation period.

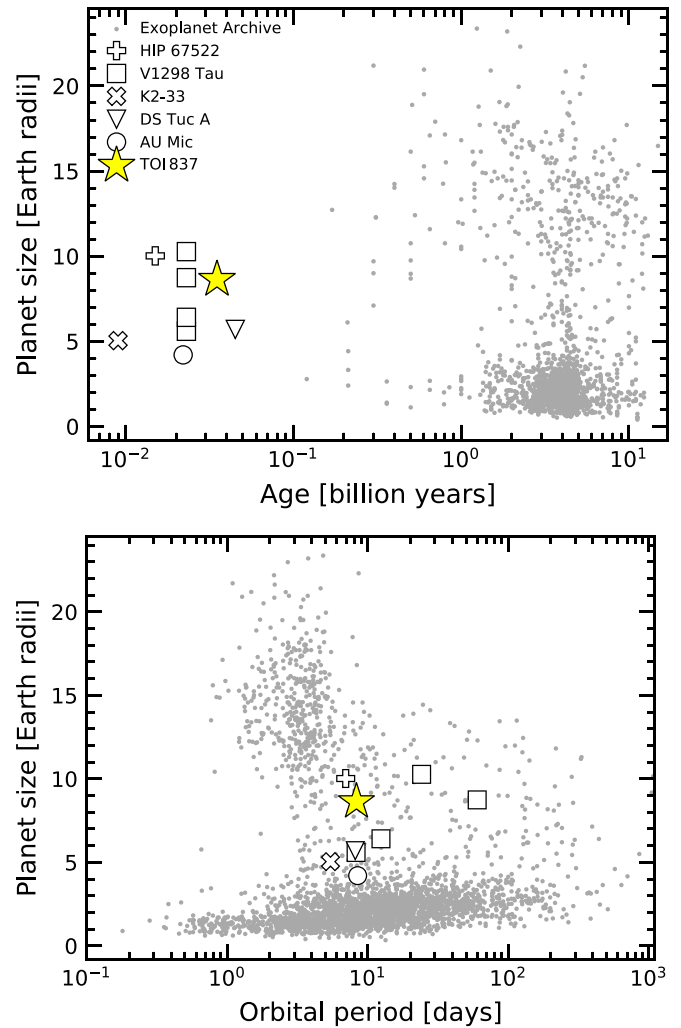


**Figure 11.** TOI 837 compared to known transiting planets. Top: Planet radii versus ages. Systems younger than 100 Myr are emphasized. The ages and radii are from the NASA Exoplanet Archive on 2020 August 27. Precise ages are known for only a small fraction of the gray points. Bottom: Planet radii versus orbital periods. The youngest known transiting planets do not obviously overlap with the population of known hot Jupiters or sub-Neptunes.

If RM measurements prove that the validated planet is real, measuring its mass may be worth the effort, because it would improve understanding of the planet’s composition and future atmospheric evolution. If an RV campaign is timed to coincide with TESS Sectors 36 and 37 (2021 March 3 through 2021 April 28), it would significantly ease extraction of the Keplerian signal. The reason is that the RVs, activity indicators, and photometry could be modeled simultaneously (e.g., Aigrain et al. 2012; Rajpaul et al. 2015). Combining photometric and RV data from non-overlapping epochs would also constrain the models, but perhaps not quite as convincingly.

While we hope that RV observations will be pursued, data acquired during the TESS mission extension may also help in understanding the system (Bouma et al. 2017; Huang et al. 2018b). In particular, additional photometry will likely enable more detailed exploration of whether the orbit of TOI 837 is eccentric and also whether the system could host additional transiting planets.

The authors thank K. Anderson for fruitful discussions and are also grateful to the anonymous referee for their constructive comments and suggestions. L.G.B. and J.H. acknowledge support by the TESS Guest Investigator Program, program G011103, through NASA grant 80NSSC19K0386. This study was based in part on observations at CTIO at the National Science Foundation's NOIRLab (NOIRLab Prop. ID 2020A-0146; principal investigator: L. Bouma), which is managed by the Association of Universities for Research in Astronomy under a cooperative agreement with the National Science Foundation. This paper includes data collected by the TESS mission, which are publicly available from MAST. Funding for the TESS mission is provided by NASA's Science Mission Directorate. TOI 837 was included on the TESS 2 minute target list thanks in part to the Guest Investigator program of G. Sacco (G011265).

The ASTEP project acknowledges support from the French and Italian polar agencies, IPEV and PNRA, and from Université Côte d'Azur under Idex UCAJEDI (ANR-15-IDEX-01). We thank the dedicated staff at Concordia for their continuous presence and support throughout the austral winter. This research received funding from the European Research Council under the European Union's Horizon 2020 research and innovation program (grant no. 803193/BEBOP) and from the Science and Technology Facilities Council (grant no. ST/S00193X/1).

This research was based in part on observations obtained at the SOAR telescope, which is a joint project of Ministério da Ciência, Tecnologia e Inovações (Laboratório Nacional de Astrofísica) do Brasil, the US National Science Foundation's NOIRLab, the University of North Carolina at Chapel Hill, and Michigan State University.

This research made use of the Exoplanet Follow-up Observation Program website, which is operated by the California Institute of Technology, under contract with NASA under the Exoplanet Exploration Program.

This research made use of the SVO Filter Profile Service (<http://svo2.cab.inta-csic.es/theory/fps/>) supported from the Spanish Ministry of Economy and Competitiveness through grant AYA2017-84089.

Resources supporting this work were provided by the NASA High-End Computing Program through the NASA Advanced Supercomputing Division at Ames Research Center for the production of the SPOC data products.

A.J. and R.B. acknowledge support from project IC120009 "Millennium Institute of Astrophysics" of the Millennium Science Initiative, Chilean Ministry of Economy. A.J. acknowledges additional support from El Fondo Nacional de Desarrollo Científico y Tecnológico (FONDECYT) project 1171208. J.I. V acknowledges support from CONICYT-PFCHA/Doctorado Nacional-21191829. R.B. acknowledges support from FONDECYT Post-doctoral Fellowship Project 3180246. C.T. and C. B acknowledge support from Australian Research Council grants LE150100087, LE160100014, LE180100165, DP170103491, and DP190103688. C.Z. is supported by a Dunlap Fellowship at the Dunlap Institute for Astronomy & Astrophysics, funded through an endowment established by the Dunlap family and the University of Toronto. D.D. acknowledges support through TESS Guest Investigator Program grant 80NSSC19K1727.

*Facilities:* *Astrometry:* Gaia (Gaia Collaboration et al. 2016, 2018). *Imaging:* Second Generation Digitized Sky Survey, SOAR (HRCam; Tokovinin 2018). *Spectroscopy:* CTIO 1.5 m

(CHIRON; Tokovinin et al. 2013), MPG 2.2 m (FEROS; Kaufer et al. 1999), AAT (Veloce; Gilbert et al. 2018). *Photometry:* ASTEP: 0.40 m (ASTEP400), El Sauce: 0.356 m, TESS (Ricker et al. 2015).

*Software:* arviz (Kumar et al. 2019), astrobases (Bhatti et al. 2018), AstroImageJ (Collins et al. 2017), astropy (Astropy Collaboration et al. 2018), astroquery (Ginsburg et al. 2018), ceres (Brahm et al. 2017), cdips-pipeline (Bhatti et al. 2019), corner (Foreman-Mackey 2016), exoplanet (Foreman-Mackey et al. 2020) and its dependencies (Kipping 2013; Theano Development Team 2016; Luger et al. 2019; Agol et al. 2020), IDL Astronomy User's Library (Landsman 1995), IPython (Pérez & Granger 2007), isochrones (Morton 2015b), lightkurve (Lightkurve Collaboration et al. 2018), matplotlib (Hunter 2007), MESA (Paxton et al. 2011, 2013, 2015), numpy (van der Walt et al. 2011), pandas (McKinney 2010), pyGAM (Servén et al. 2018), PyMC3 (Salvatier et al. 2016), radvel (Fulton et al. 2018), scipy (Jones et al. 2001), tesscut (Brasseur et al. 2019), VESPA (Morton 2012, 2015a), webplotdigitizer (Rohatgi 2019), wotan (Hippke et al. 2019).

## ORCID iDs

L. G. Bouma  <https://orcid.org/0000-0002-0514-5538>  
 J. D. Hartman  <https://orcid.org/0000-0001-8732-6166>  
 R. Brahm  <https://orcid.org/0000-0002-9158-7315>  
 P. Evans  <https://orcid.org/0000-0002-5674-2404>  
 K. A. Collins  <https://orcid.org/0000-0001-6588-9574>  
 G. Zhou  <https://orcid.org/0000-0002-4891-3517>  
 P. Sarkis  <https://orcid.org/0000-0001-8128-3126>  
 S. N. Quinn  <https://orcid.org/0000-0002-8964-8377>  
 J. Livingston  <https://orcid.org/0000-0002-4881-3620>  
 C. Bergmann  <https://orcid.org/0000-0003-2989-7774>  
 K. G. Stassun  <https://orcid.org/0000-0002-3481-9052>  
 W. Bhatti  <https://orcid.org/0000-0002-0628-0088>  
 J. N. Winn  <https://orcid.org/0000-0002-4265-047X>  
 G. Á. Bakos  <https://orcid.org/0000-0001-7204-6727>  
 N. Crouzet  <https://orcid.org/0000-0001-7866-8738>  
 G. Dransfield  <https://orcid.org/0000-0002-3937-630X>  
 T. Guillot  <https://orcid.org/0000-0002-7188-8428>  
 D. Mékarnia  <https://orcid.org/0000-0001-5000-7292>  
 A. H. M. J. Triaud  <https://orcid.org/0000-0002-5510-8751>  
 C. G. Tinney  <https://orcid.org/0000-0002-7595-0970>  
 N. Espinoza  <https://orcid.org/0000-0001-9513-1449>  
 A. Jordán  <https://orcid.org/0000-0002-5389-3944>  
 M. Barbieri  <https://orcid.org/0000-0001-8362-3462>  
 T. Trifonov  <https://orcid.org/0000-0002-0236-775X>  
 J. I. Vines  <https://orcid.org/0000-0002-1896-2377>  
 M. Vuckovic  <https://orcid.org/0000-0001-8339-6423>  
 C. Ziegler  <https://orcid.org/0000-0002-0619-7639>  
 N. Law  <https://orcid.org/0000-0001-9380-6457>  
 A. W. Mann  <https://orcid.org/0000-0003-3654-1602>  
 G. R. Ricker  <https://orcid.org/0000-0003-2058-6662>  
 R. Vanderspek  <https://orcid.org/0000-0001-6763-6562>  
 J. M. Jenkins  <https://orcid.org/0000-0002-4715-9460>  
 C. J. Burke  <https://orcid.org/0000-0002-7754-9486>  
 D. Dragomir  <https://orcid.org/0000-0003-2313-467X>  
 A. M. Levine  <https://orcid.org/0000-0001-8172-0453>  
 J. E. Rodriguez  <https://orcid.org/0000-0001-8812-0565>  
 J. C. Smith  <https://orcid.org/0000-0002-6148-7903>  
 B. Wöhler  <https://orcid.org/0000-0002-5402-9613>

## References

- Abe, L., Gonçalves, I., Agabi, A., et al. 2013, *A&A*, **553**, A49
- Addison, B. C., Horner, J., Wittenmyer, R. A., et al. 2020, arXiv:2006.13675
- Agol, E., Luger, R., & Foreman-Mackey, D. 2020, *AJ*, **159**, 123
- Aigrain, S., Hodgkin, S., Irwin, J., et al. 2007, *MNRAS*, **375**, 29
- Aigrain, S., Pont, F., & Zucker, S. 2012, *MNRAS*, **419**, 3147
- Angus, R., Aigrain, S., Foreman-Mackey, D., & McQuillan, A. 2015, *MNRAS*, **450**, 1787
- Astropy Collaboration, Price-Whelan, A. M., Sipőcz, B. M., et al. 2018, *AJ*, **156**, 123
- Bakos, G. A., Pál, A., Latham, D. W., Noyes, R. W., & Stefanik, R. P. 2006, *ApJL*, **641**, L57
- Baraffe, I., Chabrier, G., Barman, T. S., Allard, F., & Hauschildt, P. H. 2003, *A&A*, **402**, 701
- Baratella, M., D'Orazi, V., Carraro, G., et al. 2020, *A&A*, **634**, A34
- Barnes, S. A., Weingrill, J., Granzer, T., Spada, F., & Strassmeier, K. G. 2015, *A&A*, **583**, A73
- Barragán, O., Aigrain, S., Kubyskhina, D., et al. 2019, *MNRAS*, **490**, 698
- Berger, T. A., Howard, A. W., & Boesgaard, A. M. 2018, *ApJ*, **855**, 115
- Berger, T. A., Huber, D., Gaidos, E., van Saders, J. L., & Weiss, L. M. 2020, *AJ*, **160**, 108
- Bhatti, W., Bouma, L., & Yee, S. 2019, cdips-pipeline v0.1.0, Zenodo, doi:10.5281/zenodo.3370324
- Bhatti, W., Bouma, L. G., & Wallace, J. 2018, astrobase, 0.3.20, Zenodo, doi:10.5281/zenodo.1469822
- Biddle, L. I., Johns-Krull, C. M., Llama, J., Prato, L., & Skiff, B. A. 2018, *ApJL*, **853**, L34
- Bonomo, A. S., Desidera, S., Benatti, S., et al. 2017, *A&A*, **602**, A107
- Borucki, W. J., Koch, D., Basri, G., et al. 2010, *Sci*, **327**, 977
- Bossini, D., Vallenari, A., Bragaglia, A., et al. 2019, *A&A*, **623**, A108
- Bouma, L. G., Hartman, J. D., Bhatti, W., Winn, J. N., & Bakos, G. Á 2019, *ApJS*, **245**, 13
- Bouma, L. G., Winn, J. N., Kosiarek, J., & McCullough, P. R. 2017, arXiv:1705.08891
- Brahm, R., Espinoza, N., Jordán, A., et al. 2019, *AJ*, **158**, 45
- Brahm, R., Jordán, A., & Espinoza, N. 2017, *PASP*, **129**, 034002
- Brasseur, C. E., Phillip, C., Fleming, S. W., Mullally, S. E., & White, R. L. 2019, Astrocut: Tools for Creating Cutouts of TESS Images, Astrophysics Source Code Library, ascl:1905.007
- Bravi, L., Zari, E., Sacco, G. G., et al. 2018, *A&A*, **615**, A37
- Bressan, A., Marigo, P., Girardi, L., et al. 2012, *MNRAS*, **427**, 127
- Brucalassi, A., Koppenhoefer, J., Saglia, R., et al. 2017, *A&A*, **603**, A85
- Buchhave, L. A., Bakos, G. A., Hartman, J. D., et al. 2010, *ApJ*, **720**, 1118
- Burke, C. J., Gaudi, B. S., DePoy, D. L., & Pogge, R. W. 2006, *AJ*, **132**, 210
- Cameron, A. G. W., & Ward, W. R. 1976, *LPI*, **7**, 120
- Cantat-Gaudin, T., Jordi, C., Vallenari, A., et al. 2018, *A&A*, **618**, A93
- Canup, R. M., & Asphaug, E. 2001, *Natur*, **412**, 708
- Castelli, F., & Kurucz, R. L. 2004, arXiv:astro-ph/0405087
- Chatterjee, S., Ford, E. B., Matsumura, S., & Rasio, F. A. 2008, *ApJ*, **686**, 580
- Chen, Y., Bressan, A., Girardi, L., et al. 2015, *MNRAS*, **452**, 1068
- Chen, Y., Girardi, L., Bressan, A., et al. 2014, *MNRAS*, **444**, 2525
- Choi, J., Dotter, A., Conroy, C., et al. 2016, *ApJ*, **823**, 102
- Ciardi, D. R., Crossfield, I. J. M., Feinstein, A. D., et al. 2018, *AJ*, **155**, 10
- Claret, A. 2017, *A&A*, **600**, A30
- Collins, K. A., Kielkopf, J. F., Stassun, K. G., & Hessman, F. V. 2017, *AJ*, **153**, 77
- Cropper, M., Katz, D., Sartoretti, P., et al. 2018, *A&A*, **616**, A5
- Crouzet, N., Chapellier, E., Guillot, T., et al. 2018, *A&A*, **619**, A116
- Curtis, J. L., Agüeros, M. A., Douglas, S. T., & Meibom, S. 2019a, *ApJ*, **879**, 49
- Curtis, J. L., Agüeros, M. A., Mamajek, E. E., Wright, J. T., & Cummings, J. D. 2019b, *AJ*, **158**, 77
- Daban, J.-B., Gouvrete, C., Guillot, T., et al. 2010, *Proc. SPIE*, **7733**, 77334T
- Damasso, M., Lanza, A. F., Benatti, S., et al. 2020, *A&A*, **642**, A133
- Damiani, F., Prisinzano, L., Pillitteri, I., Micela, G., & Sciortino, S. 2019, *A&A*, **623**, A112
- Dauphas, N., & Pourmand, A. 2011, *Natur*, **473**, 489
- David, T., Hillenbrand, L., & Petigura, E. 2016, *Natur*, **534**, 658
- David, T. J., Cody, A. M., Hedges, C. L., et al. 2019b, *AJ*, **158**, 79
- David, T. J., & Hillenbrand, L. A. 2015, *ApJ*, **804**, 146
- David, T. J., Mamajek, E. E., Vanderburg, A., et al. 2018, *AJ*, **156**, 302
- David, T. J., Petigura, E. A., Luger, R., et al. 2019a, *ApJL*, **885**, L12
- de Zeeuw, P. T., Hoogerwerf, R., de Bruijne, J. H. J., Brown, A. G. A., & Blaauw, A. 1999, *AJ*, **117**, 354
- Díaz, R. F., Almenara, J. M., Santerne, A., et al. 2014, *MNRAS*, **441**, 983
- Dobbie, P. D., Lodieu, N., & Sharp, R. G. 2010, *MNRAS*, **409**, 1002
- Donati, J.-F., Bouvier, J., Alencar, S. H., et al. 2020, *MNRAS*, **491**, 5660
- Donati, J. F., Moutou, C., Malo, L., et al. 2016, *Natur*, **534**, 662
- Donati, J.-F., Semel, M., Carter, B. D., Rees, D. E., & Collier Cameron, A. 1997, *MNRAS*, **291**, 658
- Dotter, A. 2016, *ApJS*, **222**, 8
- Douglas, S. T., Agüeros, M. A., Covey, K. R., & Kraus, A. 2017, *ApJ*, **842**, 83
- Douglas, S. T., Curtis, J. L., Agüeros, M. A., et al. 2019, *ApJ*, **879**, 100
- Dullemond, C. P., & Monnier, J. D. 2010, *ARA&A*, **48**, 205
- Eastman, J., Siverd, R., & Gaudi, B. S. 2010, *PASP*, **122**, 935
- Ekström, S., Georgy, C., Eggenberger, P., et al. 2018, *A&A*, **537**, A146
- Evans, D. W., Riello, M., De Angeli, F., et al. 2012, *A&A*, **616**, A4
- Fabrycky, D., & Tremaine, S. 2007, *ApJ*, **669**, 1298
- Fedele, D., van den Ancker, M. E., Henning, T., Jayawardhana, R., & Oliveira, J. M. 2010, *A&A*, **510**, A72
- Feiden, G. A., & Chaboyer, B. 2013, *ApJ*, **779**, 183
- Flagg, L. J., Johns-Krull, C. M., Nofi, L., et al. 2019, *ApJL*, **878**, L37
- Foreman-Mackey, D. 2016, *JOSS*, **1**, 24
- Foreman-Mackey, D., Czekala, I., Luger, R., et al. 2020, exoplanet-dev/exoplanet v0.2.6, Zenodo, doi:10.5281/zenodo.1998447
- Fortney, J. J., Marley, M. S., & Barnes, J. W. 2007, *ApJ*, **659**, 1661
- Fulton, B. J., Petigura, E. A., Blunt, S., & Sinukoff, E. 2018, *PASP*, **130**, 044504
- Fulton, B. J., Petigura, E. A., Howard, A. W., et al. 2017, *AJ*, **154**, 109
- Fűrész, G., Szentgyorgyi, A. H., & Meibom, S. 2008, in Proc. ESO/Lisbon/Aveiro Conf., Precision Spectroscopy in Astrophysics, ed. N. C. Santos et al. (Berlin: Springer), 287
- Gaia Collaboration, Brown, A. G. A., Vallenari, A., et al. 2018, *A&A*, **616**, A1
- Gaia Collaboration, Prusti, T., de Bruijne, J. H. J., et al. 2016, *A&A*, **595**, A1
- Gaudi, B. S., & Winn, J. N. 2007, *ApJ*, **655**, 550
- Gelman, A., & Rubin, D. B. 1992, *StatSci*, **7**, 457
- Giacalone, S., & Dressing, C. D. 2020, arXiv:2002.00691
- Gilbert, J., Bergmann, C., Bloxham, G., et al. 2018, *Proc. SPIE*, **10702**, 107020Y
- Ginsburg, A., Sipocz, B., Madhura, P., et al. 2018, Astropy/Astroquery: V0.3.7 Release, Zenodo, doi:10.5281/zenodo.1160627
- Ginzburg, S., Schlichting, H. E., & Sari, R. 2016, *ApJ*, **825**, 29
- Girardi, L., Groenewegen, M. A. T., Hatziminaoglou, E., & da Costa, L. 2005, *A&A*, **436**, 895
- Gray, D. F. 2005, The Observation and Analysis of Stellar Photospheres (3rd ed.; Cambridge: Cambridge Univ. Press)
- Gray, R. O., & Corbally, C. J. 1994, *AJ*, **107**, 742
- Gupta, A., & Schlichting, H. E. 2019, *MNRAS*, **487**, 24
- Gupta, A., & Schlichting, H. E. 2020, *MNRAS*, **493**, 792
- Hartman, J. D., Gaudi, B. S., Holman, M. J., et al. 2009, *ApJ*, **695**, 336
- Hipke, M., David, T. J., Mulders, G. D., & Heller, R. 2019, *AJ*, **158**, 143
- Hirano, T., Krishnamurthy, V., Gaidos, E., et al. 2020, *ApJL*, **899**, L13
- Hoffman, M. D., & Gelman, A. 2014, *JMLR*, **15**, 1593
- Howard, A. W., Marcy, G. W., Bryson, S. T., et al. 2012, *ApJS*, **201**, 15
- Howell, S. B., Sobek, C., Haas, M., et al. 2014, *PASP*, **126**, 398
- Huang, C. X., Burt, J., Vanderburg, A., et al. 2018a, *ApJL*, **868**, L39
- Huang, C. X., Shporer, A., Dragomir, D., et al. 2018b, arXiv:1807.11129
- Hunter, J. D. 2007, *CSE*, **9**, 90
- Irwin, J., & Bouvier, J. 2009, in Proc. IAU Symp. 258, The Ages of Stars, ed. E. E. Mamajek, D. R. Soderblom, & R. F. G. Wyse (Cambridge: Cambridge Univ. Press), 363
- Irwin, J., Irwin, M., Aigrain, S., et al. 2007, *MNRAS*, **375**, 1449
- Jenkins, J. M., Twicken, J. D., McCauliff, S., et al. 2016, *Proc. SPIE*, **9913**, 99133E
- Jensen, E. 2013, Tapir: A web interface for transit/eclipse observability, Astrophysics Source Code Library, ascl:1306.007
- Johns-Krull, C. M., McLane, J. N., Prato, L., et al. 2016, *ApJ*, **826**, 206
- Jones, E., Oliphant, T., Peterson, P., et al. 2001, Open Source Scientific Tools for Python, <http://www.scipy.org/>
- Jordán, A., Brahm, R., Espinoza, N., et al. 2020, *AJ*, **159**, 145
- Kafer, A., Stahl, O., Tubbesing, S., et al. 1999, *Msngr*, **95**, 8
- Kharchenko, N. V., Piskunov, A. E., Röser, S., Schilbach, E., & Scholz, R.-D. 2005, *A&A*, **438**, 1163
- Kharchenko, N. V., Piskunov, A. E., Schilbach, E., Röser, S., & Scholz, R.-D. 2013, *A&A*, **558**, A53
- King, G. W., & Wheatley, P. J. 2020, arXiv:2007.13731
- Kipping, D. M. 2013, *MNRAS*, **435**, 2152
- Kleine, T., Touboul, M., Bourdon, B., et al. 2009, *GeCoA*, **73**, 5150
- König, S., Münker, C., Hohl, S., et al. 2011, *GeCoA*, **75**, 2119
- Kounkel, M., & Covey, K. 2019, *AJ*, **158**, 122

- Krumholz, M. R., McKee, C. F., & Bland-Hawthorn, J. 2019, *ARA&A*, **57**, 227
- Kumar, R., Carroll, C., Hartikainen, A., & Martin, O. A. 2019, *JOSS*, **4**, 1143
- Kurucz, R. L. 2013, ATLAS12: Opacity Sampling Model Atmosphere Program, Astrophysics Source Code Library, ascl:1303.024
- Lada, C. J., & Lada, E. A. 2003, *ARA&A*, **41**, 57
- Landsman, W. B. 1995, in ASP Conf. Ser. 77, *Astronomical Data Analysis Software and Systems IV*, ed. R. A. Shaw, H. E. Payne, & J. J. E. Hayes (San Francisco, CA: ASP), 437
- Li, J., Tenenbaum, P., Twicken, J. D., et al. 2019, *PASP*, **131**, 024506
- Lightcurve Collaboration, Cardoso, J. V. d. M., Hedges, C., et al. 2018, *Lightcurve: Kepler and TESS time series analysis in Python*, Astrophysics Source Code Library, ascl:1812.013
- Lin, D. N. C., Bodenheimer, P., & Richardson, D. C. 1996, *Natur*, **380**, 606
- Lindgren, L., Hernández, J., Bombrun, A., et al. 2018, *A&A*, **616**, A2
- Lithwick, Y., & Wu, Y. 2014, *PNAS*, **111**, 12610
- Livingston, J. H., Dai, F., Hirano, T., et al. 2018, *AJ*, **155**, 115
- Livingston, J. H., Dai, F., Hirano, T., et al. 2019, *MNRAS*, **484**, 8
- Lomb, N. R. 1976, *Ap&SS*, **39**, 447
- Lovis, C., & Mayor, M. 2007, *A&A*, **472**, 657
- Luger, R., Agol, E., Foreman-Mackey, D., et al. 2019, *AJ*, **157**, 64
- Malavolta, L., Nascimbeni, V., Piotto, G., et al. 2016, *A&A*, **588**, A118
- Mamajek, E. E. 2009, in AIP Conf. Proc. 1158, *Exoplanets and Disks: Their Formation and Diversity*, ed. T. Usuda, M. Tamura, & M. Ishii (New York: AIP), 3
- Mamajek, E. E., & Hillenbrand, L. A. 2008, *ApJ*, **687**, 1264
- Mann, A. W., Gaidos, E., & Ansdell, M. 2013, *ApJ*, **779**, 188
- Mann, A. W., Gaidos, E., Mace, G. N., et al. 2016a, *ApJ*, **818**, 46
- Mann, A. W., Gaidos, E., Vanderburg, A., et al. 2017, *AJ*, **153**, 64
- Mann, A. W., Johnson, M. C., Vanderburg, A., et al. 2020, *AJ*, **160**, 179
- Mann, A. W., Newton, E. R., Rizzuto, A. C., et al. 2016b, *AJ*, **152**, 61
- Mann, A. W., Vanderburg, A., Rizzuto, A. C., et al. 2018, *AJ*, **155**, 4
- Mansfield, M., Bean, J. L., Oklopčić, A., et al. 2018, *ApJL*, **868**, L34
- Marigo, P., Girardi, L., Bressan, A., et al. 2017, *ApJ*, **835**, 77
- Martio, E., Hebrard, G., Moutou, C., et al. 2020, *A&A*, **641**, L1
- Mayor, M., Marmier, M., Lovis, C., et al. 2011, arXiv:1109.2497
- McKinney, W. 2010, in Proc. 9th Python in Science Conf., ed. S. van der Walt & J. Millman (Austin, TX: SciPy), 56
- Meibom, S., Barnes, S. A., Platais, I., et al. 2015, *Natur*, **517**, 589
- Meibom, S., Torres, G., Fressin, F., et al. 2013, *Natur*, **499**, 55
- Mékarnia, D., Guillot, T., Rivet, J.-P., et al. 2016, *MNRAS*, **463**, 45
- Mermilliod, J. C. 1981, *A&A*, **97**, 235
- Miller, A. A., Irwin, J., Aigrain, S., Hodgkin, S., & Hebb, L. 2008, *MNRAS*, **387**, 349
- Mochejska, B. J., Stanek, K. Z., Sasselov, D. D., et al. 2005, *AJ*, **129**, 2856
- Mochejska, B. J., Stanek, K. Z., Sasselov, D. D., et al. 2006, *AJ*, **131**, 1090
- Montet, B. T., Feinstein, A. D., Luger, R., et al. 2020, *AJ*, **159**, 112
- Morbidelli, A., Lunine, J. I., O'Brien, D. P., Raymond, S. N., & Walsh, K. J. 2012, *AREPS*, **40**, 251
- Morton, T. D. 2012, *ApJ*, **761**, 6
- Morton, T. D. 2015a, VESPA: False Positive Probabilities Calculator, Astrophysics Source Code Library, ascl:1503.011
- Morton, T. D. 2015b, Isochrones: Stellar Model Grid Package, Astrophysics Source Code Library, ascl:1503.010
- Morton, T. D., Bryson, S. T., Coughlin, J. L., et al. 2016, *ApJ*, **822**, 86
- Nardiello, D., Piotto, G., Deleuil, M., et al. 2020, *MNRAS*, **495**, 4924
- Netopil, M., Paunzen, E., Heiter, U., & Soubiran, C. 2016, *A&A*, **585**, A150
- Newton, E. R., Mann, A. W., Tofflemire, B. M., et al. 2019, *ApJL*, **880**, L17
- Obermeier, C., Henning, T., Schlieder, J. E., et al. 2016, *AJ*, **152**, 223
- Oh, S., Price-Whelan, A. M., Hogg, D. W., Morton, T. D., & Spergel, D. N. 2017, *AJ*, **153**, 257
- Oklopčić, A., & Hirata, C. M. 2018, *ApJL*, **855**, L11
- Owen, J. E., & Wu, Y. 2013, *ApJ*, **775**, 105
- Owen, J. E., & Wu, Y. 2017, *ApJ*, **847**, 29
- Palle, E., Oshagh, M., Casasayas-Barris, N., et al. 2020, arXiv:2006.13609
- Paxton, B., Bildsten, L., Dotter, A., et al. 2011, *ApJS*, **192**, 3
- Paxton, B., Cantiello, M., Arras, P., et al. 2013, *ApJS*, **208**, 4
- Paxton, B., Marchant, P., Schwab, J., et al. 2015, *ApJS*, **220**, 15
- Pepper, J., Stanek, K. Z., Pogge, R. W., et al. 2008, *AJ*, **135**, 907
- Pérez, F., & Granger, B. E. 2007, *CSE*, **9**, 21
- Petigura, E. A., Marcy, G. W., Winn, J. N., et al. 2018, *AJ*, **155**, 89
- Plavchan, P., Barclay, T., Gagné, J., et al. 2020, *Natur*, **582**, 497
- Pollack, J. B., Hubickyj, O., Bodenheimer, P., et al. 1996, *Icar*, **124**, 62
- Quinn, S. N., White, R. J., Latham, D. W., et al. 2012, *ApJL*, **756**, L33
- Raghavan, D., McAlister, H. A., Henry, T. J., et al. 2010, *ApJS*, **190**, 1
- Rajpaul, V., Aigrain, S., Osborne, M. A., Reece, S., & Roberts, S. 2015, *MNRAS*, **452**, 2269
- Rajpurohit, A. S., Reylé, C., Allard, F., et al. 2013, *A&A*, **556**, A15
- Randich, S., Tognelli, E., Jackson, R., et al. 2018, *A&A*, **612**, A99
- Raymond, S. N., Kokubo, E., Morbidelli, A., Morishima, R., & Walsh, K. J. 2014, in *Protostars and Planets VI*, ed. H. Beuther et al. (Tucson, AZ: Univ. Arizona Press), 595
- Rebull, L. M., Stauffer, J. R., Bouvier, J., et al. 2016, *AJ*, **152**, 113
- Rebull, L. M., Stauffer, J. R., Cody, A. M., et al. 2020, *AJ*, **159**, 273
- Ricker, G. R., Winn, J. N., Vanderspek, R., et al. 2015, *JATIS*, **1**, 014003
- Rizzuto, A. C., Newton, E. R., Mann, A. W., et al. 2020, *AJ*, **160**, 33
- Rizzuto, A. C., Vanderburg, A., Mann, A. W., et al. 2018, *AJ*, **156**, 195
- Rohatgi, A. 2019, WebPlotDigitizer: v4.2., <https://automeris.io/WebPlotDigitizer>
- Salvatier, J., Wiecki, T. V., & Fonnesbeck, C. 2016, PyMC3: Python Probabilistic Programming Framework, Astrophysics Source Code Library, ascl:1610.016
- Sanchis-Ojeda, R., Winn, J. N., Marcy, G. W., et al. 2013, *ApJ*, **775**, 54
- Santerne, A., Díaz, R. F., Almenara, J.-M., et al. 2015, *MNRAS*, **451**, 2337
- Sato, B., Izumiura, H., Toyota, E., et al. 2007, *ApJ*, **661**, 527
- Scargle, J. D. 1982, *ApJ*, **263**, 835
- Seager, S., & Mallén-Ornelas, G. 2003, *ApJ*, **585**, 1038
- Servén, D., Brummitt, C., & Abedi, H. 2018, dswh/pyGAM: v0.8.0, Zenodo, doi:10.5281/zenodo.1476122
- Skutskie, M. F., Cutri, R. M., Stiening, R., et al. 2006, *AJ*, **131**, 1163
- Skumanich, A. 1972, *ApJ*, **171**, 565
- Smith, J. C., Morris, R. L., Jenkins, J. M., et al. 2016, *PASP*, **128**, 124501
- Smith, J. C., Stumpe, M. C., Cleve, J. E. V., et al. 2012, *PASP*, **124**, 1000
- Soderblom, D. R. 2010, *ARA&A*, **48**, 581
- Soderblom, D. R., Hillenbrand, L. A., Jeffries, R. D., Mamajek, E. E., & Naylor, T. 2014, in *Protostars and Planets VI*, ed. H. Beuther et al. (Tucson, AZ: Univ. Arizona Press), 219
- Spake, J. J., Sing, D. K., Evans, T. M., et al. 2018, *Natur*, **557**, 68
- Stassun, K. G., Collins, K. A., & Gaudi, B. S. 2017, *AJ*, **153**, 136
- Stassun, K. G., Oelkers, R. J., Paegert, M., et al. 2019, *AJ*, **158**, 138
- Stassun, K. G., Oelkers, R. J., Pepper, J., et al. 2018, *AJ*, **156**, 102
- Stauffer, J. R., Hartmann, L. W., Prosser, C. F., et al. 1997, *ApJ*, **479**, 776
- Stauffer, J. R., Jones, B. F., Backman, D., et al. 2003, *AJ*, **126**, 833
- Stefansson, G., Mahadevan, S., Maney, M., et al. 2020, *AJ*, **160**, 192
- Stumpe, M. C., Smith, J. C., Catanzarite, J. H., et al. 2014, *PASP*, **126**, 100
- Sullivan, P. W., Winn, J. N., Berta-Thompson, Z. K., et al. 2015, *ApJ*, **809**, 77
- Theano Development Team 2016, arXiv:1605.02688
- Tokovinin, A. 2018, *PASP*, **130**, 035002
- Tokovinin, A., Fischer, D. A., Bonati, M., et al. 2013, *PASP*, **125**, 1336
- Torres, G., Fressin, F., Batalha, N. M., et al. 2011, *ApJ*, **727**, 24
- Touboul, M., Kleine, T., Bourdon, B., Palme, H., & Wieler, R. 2007, *Natur*, **450**, 1206
- Twicken, J. D., Catanzarite, J. H., Clarke, B. D., et al. 2018, *PASP*, **130**, 064502
- van Leeuwen, F. 2009, *A&A*, **497**, 209
- Vanderburg, A., Huang, C. X., Rodriguez, J. E., et al. 2019, *ApJL*, **881**, L19
- Vanderburg, A., Mann, A. W., Rizzuto, A., et al. 2018, *AJ*, **156**, 46
- VanderPlas, J. T., & Ivezić, Z. 2015, *ApJ*, **812**, 18
- van der Walt, S., Colbert, S. C., & Varoquaux, G. 2011, *CSE*, **13**, 22
- Weber, E. J., & Davis, L., Jr. 1967, *ApJ*, **148**, 217
- Williams, J. P., & Cieza, L. A. 2011, *ARA&A*, **49**, 67
- Wright, E. L., Eisenhardt, P. R. M., Mainzer, A. K., et al. 2010, *AJ*, **140**, 1868
- Wright, J. T., Marcy, G. W., Howard, A. W., et al. 2012, *ApJ*, **753**, 160
- Yu, L., Donati, J.-F., Hébrard, E. M., et al. 2017, *MNRAS*, **467**, 1342
- Zahn, J.-P. 1977, *A&A*, **500**, 121
- Žerjal, M., Ireland, M. J., Nordlander, T., et al. 2019, *MNRAS*, **484**, 4591
- Žerjal, M., Zwitter, T., Matijević, G., et al. 2017, *ApJ*, **835**, 61
- Zhou, G., Rodriguez, J. E., Vanderburg, A., et al. 2018, *AJ*, **156**, 93
- Zhou, G., Winn, J. N., Newton, E. R., et al. 2020, *ApJL*, **892**, L21
- Ziegler, C., Tokovinin, A., Briceño, C., et al. 2020, *AJ*, **159**, 19
- Zuckerman, B., & Song, I. 2004, *ARA&A*, **42**, 685